

**Ice Water Content and Reflectivity Retrieval from Cirrus Clouds
Using Millimeter-Wave Radar and In-Situ Ice Crystal Airborne
Data**

by

José Morales Fernández

A thesis submitted in partial fulfillment of the requirements for the degree of

MASTER OF SCIENCE
in
ELECTRICAL ENGINEERING

UNIVERSITY OF PUERTO RICO
MAYAGÜEZ CAMPUS
2005

Approved by:

Sandra L. Cruz-Pol, PhD
President, Graduate Committee

Date

José Colom Ustáriz, Ph.D.
Member, Graduate Committee

Date

Henrick M. Ierkic-Vidmar, Ph.D.
Member, Graduate Committee

Date

Silvestre Colón, PhD
Representative of Graduate Studies

Date

Isidoro Couvertier, PhD
Chairperson of the Department

Date

José Mari Mutt, PhD
Director of Graduate Studies

Date

ABSTRACT

Data collected in March 2000 during the Department of Energy (DOE) Atmospheric Radiation Measurement (ARM) Cloud Intensive operational period (Cloud IOP) at the Cloud and Radiation Testbed (CART) site in Lamont, Oklahoma was used to retrieve the equivalent reflectivity factor (Z_e) and ice water content (IWC) of cirrus clouds. In situ measurements of ice particles were collected using the National Center for Atmospheric Research (NCAR) Video Ice Particle Sampler (VIPS), which flew on the University of North Dakota Citation research aircraft. Ground-based vertical radar profiles were collected using the University of Massachusetts (UMass) 33GHz/95GHz Cloud Profiler Radar System (CPRS). Data from both sensors (CPRS and VIPS) was used to retrieve and compare the equivalent radar reflectivity using density models that vary with respect to the dimensions of the particles, as well as a constant density of solid ice at 33 and 95 GHz. The equivalent reflectivity that gave better agreement between instruments was the one that used the *Brown and Francis* [1995] density model. In addition, equivalent reflectivity was calculated with ice particles model of bullet shaped crystals developed with DDSCAT software and compared with the Mie (sphere shape) results. It was found that the effect of the shape was negligible at 33 GHz, but was significant at 95 GHz. Also, ice water content (IWC) was calculated for both sensors using variable density models for the ice crystals. IWC - Z_e relationships for the three densities used in this investigation were obtained at 33 GHz. The IWC - Z_e relationship obtained using *Brown and Francis* [1995] density, resulted the most reliable (the shape, and the low variability in the discrete values).

To my family, to my country and humanity . . .

ACKNOWLEDGEMENTS

During the past two years at graduate studies in the University of Puerto Rico, several persons and institutions collaborated directly and indirectly with my research; and without their support it would have been impossible for me to complete my work and studies. For this reason this section exists, to recognize your support.

The first person that I want to express a sincere acknowledgement is my advisor, Dr. Sandra Cruz-Pol because she gave me the opportunity to research under her guidance and supervision. I received motivation; encouragement and support from her during all my studies. She helps me to grow and develop my skills as an engineer and a human being; making me a more efficient person transmitting my ideas to others by any means. I also want to thank the example, motivation, inspiration and support I received from Dr. José Colom; and also for serving on my committee.

Thanks also to Dr. Rafael Rodríguez Solís for forming part of my committee during the first part of my investigation even though he was changed later, but your recommendations and corrections to some of my documents were of valuable use and importance. Thanks also to Dr. H. Mario Ierkic for serving on my committee for his guidance, motivation, encouragement and for bringing out ideas and analysis that I would have not taken into account. His judgment helps me to understand my investigation better and to ask any question that should arise regarding it.

I would like to acknowledge the Electrical and Computer Engineering Department from the University of Puerto Rico and its research centers, Cloud Microwave Measurements of Atmospheric Phenomena (CLiMMATE), NASA Tropical Center for Earth and Space Studies (TCESS) who provided the funding and the resources for the development of this research under a Grant from NASA Award NCC5-518 and by NASA Faculty Award for Research, under a Grant from NASA NAG102074. This work also made use of CASA Engineering Research Center Shared Facilities supported by the National Science Foundation under Award Number 0313747.

I want to thank my close friends for your support during graduate school. Special thanks to Jorge Trabal, José Maeso, Margarita Baquero, Mauricio Sánchez, Víctor Marrero, Juan Antonio Torres, Silvia Herrera, Antonio Amador, from UPRM. At last, I would like to thank any person or event that have influenced my life from the time I was born; because good or bad, is the accumulation of all those experiences that have driven me to become the person that I am today.

Table of Contents

ABSTRACT.....	II
ACKNOWLEDGEMENTS.....	IV
TABLE OF CONTENTS.....	VI
TABLE LIST.....	VII
FIGURE LIST.....	VIII
1 INTRODUCTION.....	2
1.1 MOTIVATION.....	2
1.2 LITERATURE REVIEW.....	5
1.3 SUMMARY OF FOLLOWING CHAPTERS.....	11
2 THEORETICAL BACKGROUND.....	13
2.1 DESCRIPTION OF THE INSTRUMENTS USED IN THE INVESTIGATION.....	13
2.1.1 <i>NCAR Video Ice Particle Sampler (VIPS)</i>	13
2.1.2 <i>UMass Cloud Profiler Radar System (CPRS)</i>	14
2.2 REFLECTIVITY RELATED EQUATIONS.....	15
2.2.1 <i>Mie Backscattering</i>	15
2.2.2 <i>Density and Equivalent Reflectivity</i>	17
2.3 DISCRETE DIPOLE APPROXIMATION (DDA).....	19
3 EXPERIMENT SETUP AND REFLECTIVITY CALCULATIONS.....	21
3.1 METHODOLOGY FOR THE SPATIAL AND TEMPORAL MATCHING.....	21
3.2 EQUIVALENT REFLECTIVITY COMPARISON.....	26
4 ICE CRYSTALS' SHAPE EFFECT IN RADAR MEASUREMENTS.....	34
4.1 SIMULATION OF BULLET SHAPE.....	34
4.1.1 <i>DDSCAT Program and Bullet Shape Parameters</i>	34
4.1.2 <i>Bullet Backscattering vs Mie Backscattering comparison</i>	38
4.2 EQUIVALENT REFLECTIVITY FROM VIPS BULLET SIMULATED PARTICLES.....	42
5 ICE WATER CONTENT (IWC) RETRIEVAL.....	44
5.1 <i>IWC</i> DERIVATION FOR THE VIPS DATA.....	44
6 CONCLUSIONS AND FUTURE WORK.....	48
APPENDIX A. CPRS 95GHZ GRAPHS.....	52
APPENDIX B GRAPHS AT 33GHZ OF LESS RELEVANCE.....	55

Table List

Tables	Page
TABLE 2.1 CPRS Parameters	14
TABLE 2.2 $ K_w ^2$ for water at 0°C for several radar bands	18
TABLE 3.1 Approximate beam diameter for several radar bands at various altitudes	22
TABLE 3.2 RMS Difference between instruments (<i>B&F</i> crystal density $\rho=0.07D^{-1.1}$) 33GHz.	33
TABLE 3.3 RMS Difference between instruments (Heymsfield density $\rho=0.78D^{-0.0038}$) 33GHz.	33
TABLE 3.4 RMS Difference between instruments (constant ice density $\rho=.916 \text{ g cm}^{-3}$) 33GHz.	33
TABLE 5.1 Coefficients <i>a</i> and <i>b</i> for the new calibrated crystal density models at 33GHz ...	45
TABLE 5.2 <i>RMS</i> results for the <i>IWC</i> models using <i>B&F</i> density model at 33GHz	47
TABLE 5.3 <i>RMS</i> results for the <i>IWC</i> models using <i>Heymsfield</i> density model at 33GHz	47
TABLE 5.4 <i>RMS</i> results for the <i>IWC</i> models using constant density at 33GHz	47

Figure List

Figures	Page
Figure 1.1 Percentage transmission through the earth’s atmosphere, along the vertical direction, under clear sky conditions [Ulaby et al., 1986]. The 35 and 90 GHz windows are easily observed where high transmission is obtained at high microwaves frequencies.	4
Figure 1.2 Dipole representation of particles. a) Spherical shape. b) Bullet shape [Villa et al., 2002]	7
Figure 1.3 Density versus diameter for the density models examined in this investigation... 10	
Figure 3.1 Experimental Setup of the devices used for comparison.....	22
Figure 3.2 a),b) and c) are VIPS location (3D, side and top view respectively) when the instrument was gathering data from 18:31:59-22:42:00 UTC for a total of 15,000 points on March 9, 2000. d) shows CPRS 33GHz data that matched in time, but the closest points between instruments at the time of the graph above (shown by red circles) are at the beginning and end of the cloud, so this day is not a good one for comparison purposes [ARM Archive].....	23
Figure 3.3 a),b) and c) are VIPS location (3D, side and top view respectively) when the instrument was gathering data from 22:22:09-25:44:20 UTC for a total of 12,132 points on March 12, 2000. d) shows CPRS 33GHz data matched in time, but the closest point between instruments at the time of the graph above (shown by a blue circle and the altitude of the plane shown by a black line) are in the cloud top region, nearly outside of the cloud, so this day is not a good one for comparison purposes [ARM Archive].	24
Figure 3.4 a),b) and c) are VIPS location (3D, side and top view respectively) when the instrument was gathering data from 19:21:23-22:29:00 UTC for a total of 15,711 points on March 13, 2000. d) shows CPRS 33GHz data matched in time, [ARM Archive]. e) is the same as d) but zoomed from 4 to 10 km and with a different color scale; the altitude of the plane is shown by a blue line and the closest points are inside the white rectangle lines, good matching in time and space was obtained for this day.....	25
Figure 3.5 (left) Average particle size distribution from data collected between the 9 and 13 of March 2000, by the University of North Dakota Citation research aircraft, using a cloud particle imagery (CPI). (right) Particle size distribution obtained from data of the VIPS when the plane flew very close to radar location.	27
Figure 3.6 Overhead view of the VIPS flight track pattern for March 13, 2000. The blue dot at (0,0) indicates the position of the CPRS radar, the blue circle is only a reference for data that were spatially closed between sensors; while the colors represent the range of equivalent reflectivity Z_e obtained using <i>B&F</i> density equation (1.2). b) Is the same as a) but in three dimensions to show the altitude variation. (<i>Brown and Francis, 1995, density model at 33GHz</i>)	28

Figure 3.7 Same as Figure 3.6 but for 95 GHz.	28
Figure 3.8 Same as Figure 3.6 but using <i>Heymsfield et al.</i> density model at 33GHz.	29
Figure 3.9 Same as Figure 3.6 but using <i>Heymsfield et al.</i> , [1972] density model at 95GHz.	29
Figure 3.10 Same as Figure 3.6 but using a constant ice density of 0.916 g/cm ³ at 33GHz.	29
Figure 3.11 Same as Figure 3.6 but using a constant solid ice density of 0.916 g/cm ³ at 95GHz.	30
Figure 3.12 Time traces of the data showing the radar reflectivity of the two channels of CPRS data during the time when the airplane over flew over the radar, the red colored is for the 95 GHz data while the blue is for the 33 GHz data.	30
Figure 3.13 Comparison between equivalent reflectivity obtained from CPRS radar and VIPS in-situ instrument, @ 7km of height over time and distance, <i>Brown and Francis</i> , 1995 density model.	31
Figure 3.14 Comparison between equivalent reflectivity obtained from radar and in-situ instrument, @ 7km of height over time and distance, using <i>Heymsfield et al.</i> , 1972 density model.	32
Figure 3.15 Comparison between equivalent reflectivity obtained from radar and in-situ instrument, @ 7km of height over time and distance, using a constant density of 0.916 g/cm ³	32
Figure 4.1 Schematics to describe the dimensions in a cirrus cloud bullet shaped particle. a) Bullet side view. b) Cross section of a bullet.	36
Figure 4.2 Methodology used to create a bullet formed by an array of N dipoles. (General process)	37
Figure 4.3 Target orientation in equation in the Lab Frame. \hat{x} is the direction of propagation of the incident radiation, and the \hat{y} is the direction of the “real” component of the first incident polarization mode. In this coordinate system, the orientation of target axis \hat{a}_1 is specified by angles Θ and Φ . With target axis \hat{a}_1 fixed, the orientation of target axis \hat{a}_2 is then determined by angle β specifying rotation of the target around \hat{a}_1 . When $\beta=0$, \hat{a}_2 lies in the \hat{a}_1, \hat{x} plane.	37
Figure 4.4 Backscattering comparison using <i>Brown and Francis</i> crystal density @ 33GHz.	39
Figure 4.5 Backscattering comparison using <i>B&F</i> density @ 95GHz.	39
Figure 4.6 Backscattering comparison using <i>Heymsfield</i> density model @ 33GHz.	40
Figure 4.7 Backscattering comparison using <i>Heymsfield</i> crystal density @ 95GHz.	40
Figure 4.8 Backscattering comparison using constant solid ice density @ 33GHz.	41
Figure 4.9 Backscattering comparison using constant solid ice density @ 95GHz.	41
Figure 4.10 a) Comparison between equivalent reflectivity obtained from radar and in-situ instrument, @ 7km of height over time and distance, using a variable density (<i>Brown and Francis</i>) of $\rho=0.07D^{-1.1}$ using backscatter simulated using DDSCAT bullet model (purple circles). b) is the same as a) but at 95 GHz.	42
Figure 4.11 a) Comparison between equivalent reflectivity obtained from radar and in-situ instrument, @ 7km of height over time and distance, with a variable density of $\rho=0.78D^{0.0038}$ (<i>Heymsfield et al.</i>) using backscatter simulated using DDSCAT bullet model (purple circles). b) is the same as a) but at 95 GHz.	43

Figure 4.12 a) Comparison between equivalent reflectivity obtained from radar and in-situ instrument, @ 7km of height over time and distance, using a constant density of $\rho=0.916$ using backscatter simulated using DDSCAT bullet model (purple circles). b) is the same as a) but at 95 GHz.	43
Figure 5.1 Various IWC models applied to the in-situ data using <i>B&F</i> ice crystal density ($\rho(D)=0.07D^{-1.1}$).....	45
Figure 5.2 Various IWC models applied to the in-situ data using <i>Heymsfield</i> et al. ice crystal density ($\rho(D)=0.78D^{-0.0038}$). The blue dots represent the IWC obtained for the VIPS data.	46
Figure 5.3 Various IWC models applied to the in-situ data using a constant density $\rho=0.916$ g/m ³	46

1 INTRODUCTION

The purpose of this study is to find cirrus cloud data which are matched in time and space with millimeter wavelength radar and an in-situ instrument, in order to compare the retrieved values of equivalent reflectivity (Z_e) and ice water content (IWC), using different density models, and taking the effects of ice particles shape into account in order to develop better estimates of Z_e and IWC for midlatitude cirrus clouds using radar measurements. This was done in three sections; the first was the calculation of equivalent reflectivity from space/time collocated data between instruments (CPRS and VIPS), using the *Brown* and *Francis* density model and *Heymsfield* et al. density model and applying this to the Mie equations for backscattering. The second part was to simulate real ice particle shapes found in cirrus clouds to obtain their backscatter behavior at 33 and 95GHz. This was done using the program DDSCAT and using *Villa* et al. bullet shape code; the calculations also use the density models mentioned above and are applied to the VIPS data in order to obtain their equivalent reflectivity. Finally IWC - Z_e relationships were derived for all these different equivalent reflectivity calculations and compared to existing models.

1.1 Motivation

Cirrus clouds play an important role in the balance of Earth's energy dynamics. They cover approximately about 20% of Earth, are formed at altitudes above 5km (16,500ft) and are mainly composed of ice particles. They cool the Earth by reflecting solar radiation back

to space and warm it by trapping infrared radiation emitted from the surface and lower atmosphere [Evans, 2001; Aydin and Walsh, 1999]. Some other facts related to these clouds are: that if there are many cirrus clouds in the sky it may be a sign that a frontal system is approaching, and that also cirrus clouds can be remnants of thunderstorms [Absolute Astronomy, 2005]. It is also important to point out that they indirectly affect the study of other systems such as marine and desert surfaces, and therefore the necessity of studying and estimating their macrophysics characteristics such as density, dimensions, and layer constitution [Schmidt, et al., 1993].

In order to validate the representation of cirrus clouds in global circulation models used for climate research and weather forecasting there is a requirement to obtain global data on the vertical structure of ice water content (*IWC*) [Liu and Illingworth, 1999]. Most of these experiments employed various types of instruments, such as radars and in-situ devices whose measurements result too expensive and also cover a limited region of the sky, which in turn reinforces the intention of validating radar data [El-Magd et al., 2000].

Proper understanding of cirrus clouds properties requires retrievals from remote sensing instruments. Appropriate radars for studying cirrus clouds are millimeter wavelength radars such as the UMass Cloud Profiler Radar System (CPRS), because they are sensitive enough to study particles smaller than one millimeter; while an in-situ instrument such as the NCAR Video Ice Particle Sampler (VIPS) is appropriate to compare and validate data from the radar. The CPRS operating frequencies are 33 and 95 GHz, which lie within atmospheric windows, (see Figure 1.1) making it useful for studying the microphysical properties of clouds [Sekelsky and McIntosh, 1996]. Data from both instruments were obtained on March 2000 as

a result of the ARM experiment at the Southern Great Plains (SGP) site in Oklahoma [http://www.archive.arm.gov/].

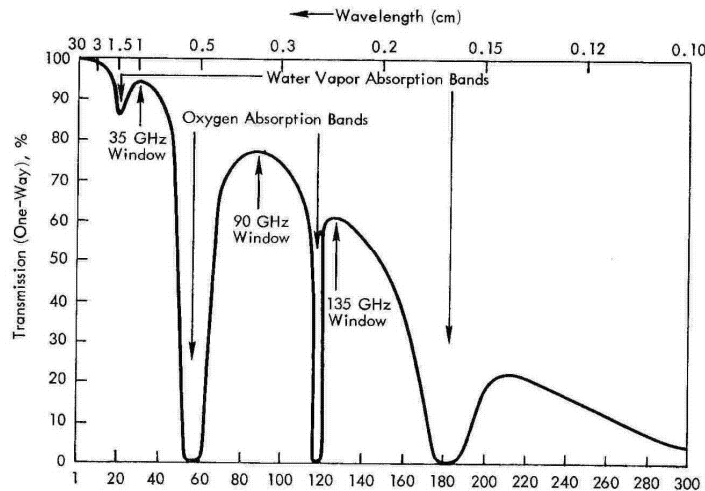


Figure 1.1 Percentage transmission through the earth's atmosphere, along the vertical direction, under clear sky conditions [Ulaby et al., 1986]. The 35 and 90 GHz windows are easily observed where high transmission is obtained at high microwaves frequencies.

Scattering behavior from cirrus clouds ice particles using millimeter wavelength radars is known to depend on size, density, shape and radar wavelength. It is known that the shapes of the particles found in cirrus clouds are not spherical (bullets and bullet rosettes are the most common) yet for many applications the use of Mie scattering, which assumes a sphere shape for the particles, is a good approximation. But this assumption on occasions can lead to incorrect scattering properties and also even some times, polarization parameters are neglected [Lemke et al., 1998]. The density of the ice particles has been shown to have a big effect in the backscattering [Villa et al., 2002; Heymsfield et al., 2004]. With knowledge of density and measurements or representations of ice particle size distribution (PSD), many ice

cloud bulk properties such as *IWC* and the equivalent radar reflectivity, can be derived [Heymsfield et al., 2004].

One of the most common methods employed to evaluate the effects of particles shape on the backscattering efficiency is the discrete dipole approximation (DDA); this can be accomplished using software such as DDSCAT [Draine and Flatau, 2001]. DDA changes in backscattering due to shape (e.g. bullet or bullet rosette) of the ice particles can be compared with backscattering obtained using Mie or Rayleigh and using constant or variable density; a variable density is expected to change the values of equivalent reflectivity and *IWC*.

Finally, this work will serve to develop a better understanding and characterization of cirrus clouds microphysical and radiative properties which could facilitate in the future the retrieval of equivalent reflectivity and *IWC* using millimeter wavelength radars.

1.2 Literature Review

One of the major problems in atmospheric science today is remotely estimating cloud microphysical and macrophysical properties, which are required to improve models of cloud radiative behavior [Simpson et al., 2001].

Several experiments have been done in the past two decades to improve the understanding of the relationship between microphysical and radiative properties of cirrus clouds e.g. FIRE-I, FIRE-II and ARM. To accomplish this, radar and in-situ measurements had been analyzed and compared; e.g. *El-Magd* et al. [2000] has documented comparisons for graupel and hail.

From different studies it has been shown that successful estimate of microphysical properties from precipitating clouds and other clouds with high liquid water content, can be obtained using radars that operate at frequencies lower than 12 GHz; but when studying cirrus clouds these radars do not yield good estimates [*Clothiaux et al., 1995*]. However millimeter wave radars operated at frequencies within the atmospheric windows (35, 94, 140, and 220 GHz) have proven to be sensitive at studying particles smaller than 1mm, which are the most common sizes found in cirrus clouds ice particles [*Sekelsky and McIntosh, 1996*]. A radar system that can operate in two atmospheric windows and is useful for cirrus clouds studies is the UMass Cloud Profiling Radar System (CPRS). The CPRS operates at 33 and 95 GHz; more information and characteristics of this radar are described in the following chapters.

For in-situ measurements of microphysical properties in cirrus clouds the NCAR Video Ice Particle Sampler (VIPS) was employed. This device uses an electro-optical instrument used to collect and record a continuous sample of cloud particles down to 5 μm . Particle concentration retrievals can be obtained with this type of instrument which serves to obtain information of quantities such as equivalent reflectivity (Z_e) and ice water content (IWC). More information regarding this instrument can be found in the following sections.

Evans and Vivekanandan [1990] have shown that radar reflectivity is dependent of shape, size and other microphysical properties. As was mentioned in previous sections the shape can be taken into account using software such as DDSCAT; which uses the discrete dipole approximation (DDA) method to calculate the backscattering efficiency from irregular geometric shapes such as ice particles. A quick description of what DDA does in order to

calculate a parameter such as the backscatter efficiency is the following: it represents a random shaped particle by a finite array of N dipolar subunits arranged on a cubic lattice as shown in Fig. 1.2.a and b. For every dipole an electric field is calculated and the backscattering is calculated from the sum of all the fields due to each dipole. More information regarding DDA can be found in later sections.

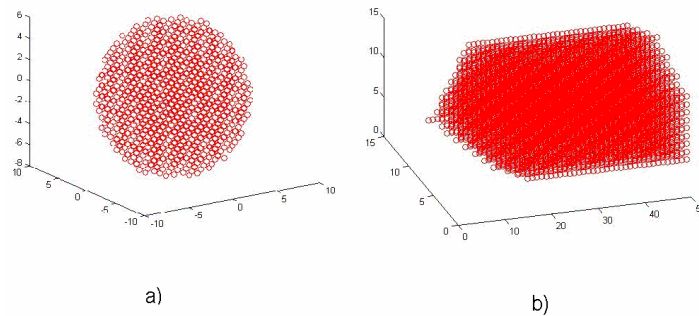


Figure 1.2 Dipole representation of particles. a) Spherical shape. b) Bullet shape [Villa et al., 2002]

Simulations from electromagnetic scattering of ice particles using Discrete Dipole Approximation (DDA), assuming hexagonal plates and columns, use constant values for the bulk density (0.92 g/cm^3), index of refraction (at -20°C ; $m= 1.784 - j0.0016$ for 37 GHz) [Evans and Vivekanandan, 1990]. This study found that the results were dependent on these values mostly on the crystal bulk density, previously assumed constant.

Dungey and Bohren [1993] analyzed backscattering produced by the ice particles with a 94 GHz signal at different angles and with vertical polarization using Coupled-Dipole Method, with the same principle as the DDA. They assumed a constant index of refraction of $1.878 + j0.000476$ for a temperature of 0°C , and used hexagonal prismatic as the shape for the ice crystals. They found that the backscattering varies significantly with respect to the

angle of incidence of the signal, although changes in polarization were found to have insignificant effects [Dungey and Bohren, 1993].

Tang and Aydin [1995] performed scattering studies of ice at 94 and 220 GHz using the Finite Difference Time Domain (FDTD) method to simulate the scattering of ice crystals particles [Aydin and Tang, 1997a; 1997b]. They used geometric models for crystals such as hexagonal plate, stellar crystal and the hexagonal column given by Auer and Veal [1970]. A constant ice density of 0.9 g cm^{-3} was used for the three models, constant permittivity of $3.1307 - j0.0047$ was assumed, for 94 and 220 GHz, [Ray, 1972; Bohren and Battan, 1982]. The study was made for crystals sizes between 100 and 200 μm . Different scattering characteristics among the shapes analyzed were found when observing the dual frequency ratio (DFR); in addition the linear depolarization ratio versus elevation angle was found to be comparable for the stellar crystals and the hexagonal plates, and significantly different for the columns. They concluded that the ice crystals observations at different elevation angles can be used to discriminate between the plates and columns efficiently.

Sekelsky et al. [1998; 1999] used simulations from the ice crystals backscattering at various millimeter wavelengths using the DDA on the version 5^a of DDSCAT, using variable density models. They calculated the dual-wavelength ratio (DWR). Their findings also agree with previous studies where the shape and orientation are the principal causes of error on the DWR estimates and other products.

There are few studies that consider the shape of a bullet or a bullet rosette, e.g., [Aydin and Walsh, 1996; 1999]. They made simulations implementing the geometric shape of a bullet and a bullet rosette estimated by Heymsfield and Knollenberg [1972] for a temperature

range between -18° and -20° °C, but, they used a constant density of 0.9 g cm^{-3} , which is considered appropriate for temperatures between -9.3° to -3.5° C.

Liu and Illingworth [1999] on other hand concluded that the precise shape of ice particles can be neglected when calculating radar reflectivity. Their justification for this was that the larger particles that contribute most to the reflectivity have a lower density and therefore reduced refractive index so they effectively reflect microwaves as if they were spherical. They consider that the density $\rho(D)$ has a stronger influence in the Z_e and IWC calculations. The following crystal density models are the most commonly used for ice particles as the ones present in cirrus clouds and Figure 1.3 shows the behavior of these density models as well as one of constant density of 0.916 g/cm^3 :

$$\rho(D) = 0.78D^{-0.0038} \text{ [g/cm}^3\text{]} \quad \textit{Heymsfield et al.} \quad [1972] \quad \mathbf{1.1}$$

$$\rho(D) = 0.07D^{-1.1} \text{ [g/cm}^3\text{]} \quad \textit{Brown and Francis} \quad [1995] \quad \mathbf{1.2}$$

this is for particles larger than $100\mu\text{m}$ and density of solid ice (0.916g/cm^3) for smaller particles.

$$\rho(D) = 0.916 \text{ [g/cm}^3\text{]} \quad \mathbf{1.3}$$

where D is in mm.

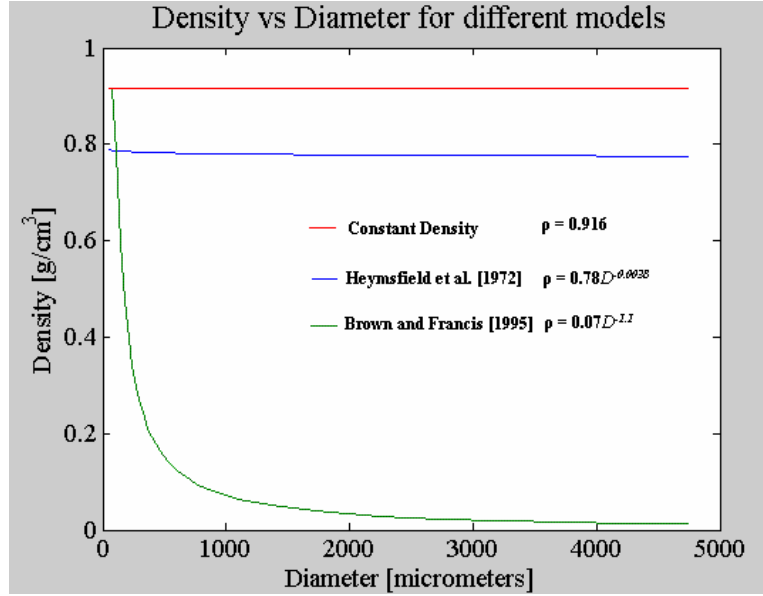


Figure 1.3 Density versus diameter for the density models examined in this investigation.

IWC models for cirrus clouds of the form $IWC = aZ_e^b$ have been obtained for different campaigns such as Central Equatorial Pacific Experiment (CEPEX), European Cirrus and Radiation Experiment (EUCREX), FIRE-I, etc. Some of the most important models are:

$$IWC = 0.0977Z_e^{0.596} \quad [\text{g/m}^3] \quad \text{Liu and Illingworth [1999]} \quad \mathbf{1.4}$$

$$IWC_1 = 0.064Z_e^{0.58} \quad [\text{g/m}^3] \quad \text{Atlas et al. [1995]} \quad \mathbf{1.5}$$

$$IWC_2 = 0.15Z_e^{0.84} \quad [\text{g/m}^3] \quad \text{Liu and Illingworth [1999]} \quad \mathbf{1.6}$$

$$IWC_3 = 0.027Z_e^{0.78} \quad [\text{g/m}^3] \quad \text{Liao and Sassen [1994]} \quad \mathbf{1.7}$$

where IWC is in $\text{g} \cdot \text{m}^{-3}$ and Z_e is in $\text{mm}^6 \cdot \text{m}^{-3}$.

All of the IWC models (equations 1.4 to 1.7) are for K_a band. The model for 1.4 was obtained from aircraft data from CEPEX experiment. The model for 1.5 was obtained from the FIRE-I campaign [Atlas et al., 1995]; while model 1.7 is for data obtained in 1973-1975

by *Heymsfield and Platt* [1984] as analyzed by *Liao and Sassen* [1994]. *Liao and Sassen* [1994] assumed that all the particles had the density of solid ice (0.916 g/cm^3), although they did comment that the presence of low density relatively large particles would have a significant effect on radar-reflectivity relations. Finally the model 1.6 was obtained by *Liu and Illingworth* [1999] and is based in the *Liao and Sassen* [1994] recalculation using *Brown and Francis* [1995], (also referred to as *B&F* in this work) variable density.

Another effect that could influence Z_e - IWC relations is the polarization. The radar cross section of nonsymmetrical particles, such as bullets, columns and hexagonal plates, depends strongly on the polarization of the incident electromagnetic field and the orientation of the particle relative to the observing radar; however at zenith incidence these effects are minimal except in cases where crystals are oriented in a preferred direction by electric fields [*Metcalfe*, 1995; *Galloway et al.*, 1997]. There have not been found difference between horizontal and vertical polarized backscatter at zenith incidence for ice crystals at millimeter wavelengths. For linear polarizations, differential reflectivity is defined as the ratio of H to V polarized reflectivity, $Z_{DR}=10\log(Z_H/Z_V)$, in decibels. Models of Z_{DR} for bullets, columns, and hexagonal plates at 35, 94 and 220 GHz show substantial variation with radar elevation angle [*Aydin and Walsh*, 1996]. But at zenith incidence (the case of the CPRS in this investigation) $Z_{DR}=0$ for each crystal type.

1.3 Summary of Following Chapters

We first develop the necessary background theory in chapters 1 & 2. Chapter 3 deals with the experiment setup, and results of equivalent reflectivity. Chapter 4 presents the effect of

the shape of the ice particle in the backscattering calculation as well of its effect in the reflectivity retrieval. Chapter 5 shows results of *IWC* for the VIPS data using the three density models mentioned before and some comparisons with existing models. Conclusions and future work are presented in chapter 6.

2 THEORETICAL BACKGROUND

The spring 2000 Cloud IOP was conducted during the first three weeks of March 2000 to generate a dataset suitable for the determination of the three dimensional distribution of cloudiness and cloud properties within the experimental domain. In that month of March, pure ice clouds (cirrus) among other types of clouds were captured and documented with ground-based radars and airborne instruments [ARM website].

2.1 Description of the instruments used in the investigation

2.1.1 NCAR Video Ice Particle Sampler (VIPS)

The ice particle data was collected using an instrument called Video Ice Particle Sampler (VIPS) and given by Dr. Andrew Heymsfield from the National Center for Atmospheric Research (NCAR). This is an airborne instrument that takes samples of ice particles for sizes down to 5 μm . The VIPS uses an electro-optical and imaging unit mounted in a standard particle measurement system (PMS) container, and also has data acquisition and recording components. The particles' images are recorded in two formats, one is at 30 Hz on high-resolution Hi-8 VCRs; the other format is at 1 Hz, digitized in real-time in an Apple PowerPC [Heymsfield, 2000].

Data from this instrument is in MS Excel® table format. From this data, this study used: the altitude of the airplane, temperature of the measurement, the diameters D_m (which is the maximum dimension measured for the particle) and concentration of particles $N(D_m)$ per cubic meter present for these diameters. In addition, the times when the data was gathered

and the coordinates of the airplane were used in order to compare in time and space with the radar data.

2.1.2 UMass Cloud Profiler Radar System (CPRS)

The CPRS operates at 33 (Ka band) and 95 (W band) GHz frequencies, it possess a programmable pedestal that facilitates various scanning modes and a high speed VXI-bus-based data acquisition and digital signal processing (DSP). The 33 and 95 GHz channels transmit and receive through a single one meter diameter dielectric lens antenna; some of the most important specifications are shown in Table 2.1 [Sekelsky et al., 1999].

TABLE 2.1 CPRS Parameters

	W band	Ka band
Frequency (GHz)	95	33
Peak power (kW)	1.5	120
Average power (W)	15	120
Pulse width (ns)	500	200
Gain	$10^{5.8}$	$10^{4.83}$
Range gate spacing (m)	75	30
Pulse repetition freq. (kHz)	10	5
Noise figure (dB)	13	11
Bandwidth (MHz)	2	5
Beam width (deg)	0.18	0.50

The CPRS was zenith looking at latitude 36.6011°N and longitude 97.4809°W. The data already processed by this radar was obtained from the ARM website [<http://www.archive.arm.gov/>] with Dr. Stephen M. Sekelsky permission and is in NetCDF format; these files were opened using the IDL software. From these data we used the range (vertical distance to the radar), the time of the measurement and the equivalent reflectivity.

2.2 Reflectivity related equations

2.2.1 Mie Backscattering

The radar measures the backscatter energy received from the volume of raindrops and other types of particles such as ice crystals. There is one basic theory describing this scattering, the Mie scattering theory. A special case of Mie theory is the Rayleigh scattering, which describes scattering characteristics of particles that are much smaller than the wavelength of radiation that they come upon. Objects of this size do not scatter all wavelengths evenly. Alternately, Mie scatterers are larger in size and are able to scatter all wavelengths in all directions with measurements that give an estimate of the particle's size (comparable to the radiation wavelength) with the backscattering coefficient $\sigma_b \propto f^4$ [Ulaby et al., 1986].

The backscatter coefficient (σ_b) and the backscatter efficiency (ξ_b) are related by the following formula:

$$\sigma_b(D) = \xi_b \pi r^2, \quad [\text{mm}^2] \quad \mathbf{2.1}$$

derived from Mie's solution for the scattering and absorption of electromagnetic waves by a dielectric sphere of arbitrary radius r in mm.

From Mie's solution, the backscattering efficiency is given by [Ulaby et al., 1986]:

$$\xi_b = \frac{1}{\chi^2} \left| \sum_{l=1}^{\infty} (-1)^l (2l+1)(a_l + b_l) \right|^2 \quad \mathbf{2.2}$$

where a_l and b_l are the Mie coefficients. These coefficients are formulated in terms of

$$\chi = \frac{2\pi r}{\lambda_0} \sqrt{\varepsilon'_{rb}} \quad 2.3$$

which is the particle size with respect to the free-space wavelength λ_0 in mm, where ε'_{rb} is the real part of the relative dielectric constant of the background medium. When the background medium is air, as is true in the atmosphere, then we can assume $\varepsilon'_{rb} = 1$. Mie coefficients are also formulated in terms of

$$n = \sqrt{\varepsilon}, \quad 2.4$$

which is the refraction index, calculated in terms of ε , the permittivity for liquid water.

The expressions for a_l and b_l are

$$a_l = \frac{\left(\frac{A_l}{n} + \frac{1}{\chi}\right) \text{Re}\{W_l\} - \text{Re}\{W_{l-1}\}}{\left(\frac{A_l}{n} + \frac{l}{\chi}\right) W_l - W_{l-1}} \quad 2.5$$

$$b_l = \frac{\left(nA_l + \frac{1}{\chi}\right) \text{Re}\{W_l\} - \text{Re}\{W_{l-1}\}}{\left(nA_l + \frac{1}{\chi}\right) W_l - W_{l-1}} \quad 2.6$$

where

$$W_l = \left(\frac{2l-1}{\chi}\right) W_{l-1} - W_{l-2}, \quad 2.7$$

with

$$W_0 = \sin \chi + j \cos \chi, \quad 2.8$$

and

$$A_l = -\frac{l}{n\chi} + \left[\frac{l}{n\chi} - A_{l-1} \right]^{-1}, \quad 2.9$$

with

$$A_0 = \cot(n\chi), \quad 2.10$$

2.2.2 Density and Equivalent Reflectivity

With the matched data we will proceed to calculate the equivalent reflectivity using the Number of particles for a given diameter $N(D)$ from the VIPS data using the following equation [Sekelsky et al., 1999]:

$$Z_e = \frac{10^{12} \lambda^4}{4\pi^4 |K_w(\lambda)|^2} \int_0^{D_{\max}} \xi_b(D, \lambda, \rho) N(D) D^2 dD \quad [mm^6 m^{-3}] \quad 2.11$$

where λ is the wavelength used in (m), ξ_b is the backscattering efficiency, $N(D)$ is the particle size distribution (PSD) in ($mm^{-1}m^{-3}$), D is D_m from the VIPS in (mm) and $K_w(\lambda)$ is a dimensionless quantity called the dielectric factor given by:

$$K_w(\lambda) = \frac{n(\lambda)^2 - 1}{n(\lambda)^2 + 2} \quad 2.12$$

Where n is the complex index of refraction for water; this index is used because the true index of refraction for the media observed is typically unknown. The quantity K_w is not constant with respect to frequency; Table 2.2 shows different values of $|K_w|^2$ for the frequencies of interest; $|K_w|^2$ at 0°C is chosen because it changes slightly with temperature. As is shown in the equivalent reflectivity Z_e equation (2.11), the backscattering efficiency ξ_b which is calculated using the full Mie equations from section 2.2.1, is a function of density,

diameter and wavelength; given that we have the values of the diameters and the wavelength, we only need the values of the density of the particles. Previous studies have found that the density of ice particle varies with respect to their diameter and one of our objectives in this work was to test crystal density models from *Heymsfield et al.* and *Brown and Francis*, equations (1.1) and (1.2), respectively.

TABLE 2.2 $|K_w|^2$ for water at 0°C for several radar bands

	Ka band (33GHz)	W band (95GHz)
$ K_w ^2$	0.885	0.698

Wiener's theorem states [*Oguchi*, 1983], that the complex index of refraction, m (sometimes referred as n), depends of the bulk density when dealing with dry ice particles according to:

$$m = \sqrt{\frac{2 + n_i^2 + 2f_i(n_i^2 - 1)}{2 + n_i^2 + f_i(-n_i^2 + 1)}} \quad 2.13$$

where f_i represents a nondimensional fraction of the volume of air and ice and it is defined as:

$$f_i = \frac{\rho}{\rho_i} \quad 2.14$$

with ρ_i as the solid ice density (0.916 g cm⁻³) and where n_i is the complex index of refraction of solid ice which is different for every frequency (1.785 + j0.000235 at 33 and 1.784 + 0.00010 at 95 GHz) [*Warren*, 1984; *Ray*, 1972]. Using the above equations, we obtained an index of refraction for each frequency and each size.

2.3 Discrete Dipole Approximation (DDA)

In recent years, the DDA, or coupled dipole-method, has shown high potential for computing scattering and absorption by a target of arbitrary shape, being especially suited for investigations in the resonance region where the particle size is of the same order as the wavelength [Lemke et al., 1998].

As was mentioned in the literature review section, the basic idea of the DDA is the representation of an arbitrary particle by a finite array of N dipolar subunits arranged on a cubic lattice. These subunits are sufficiently small to give rise to only electric dipole radiation; the dipoles may be contemplated as representing the polarizability of a particular subvolume of the target material. The substitution requires specification of the geometry (location of the dipoles) and the dipole polarizabilities α_{ij} . Each dipole $\mathbf{P}_j = \alpha_j \mathbf{E}_j$ is then subject to incident field $\mathbf{E}_{inc,j}$ as well as to the field due to the other excited dipolar subunits,

$$\mathbf{E}_j = \mathbf{E}_{inc,j} - \sum_{k \neq j}^N A_{jk} \mathbf{P}_k \quad 2.15$$

where $-A_{jk} \mathbf{P}_k$ is the electric field at r_j due to dipole \mathbf{P}_k at location r_k , including retardation effects. Each element A_{jk} is a 3x3 matrix describing the field geometry, for that reason it contains the particle information. By defining $A_{jj} \equiv \alpha_j^{-1}$, the scattering problem reduces to finding the polarizations \mathbf{P}_j satisfying a system of $3N$ complex linear equations:

$$\sum_{k=1}^N A_{jk} \mathbf{P}_k = \mathbf{E}_{inc,j} \quad 2.16$$

Complex conjugate gradient (CGM) methods, which have proven to be effective and efficient for finding \mathbf{P} iteratively, are implemented, because for a general geometry, solving

equation 2.14 via inversion methods is not practicable. The incorporated FFT drastically reduces the required number of operations, but confines to dipole locations on a periodic lattice. By estimation of \mathbf{P} for two orthogonal vectors of polarization \mathbf{e}_h , \mathbf{e}_v of the incident field, the complete amplitude scattering matrix is determined for a particular scattering direction:

$$\begin{pmatrix} E_{sca,h} \\ E_{sca,v} \end{pmatrix} = -\frac{j e^{jkr}}{kr} \begin{pmatrix} S_2 & S_3 \\ S_4 & S_1 \end{pmatrix} \begin{pmatrix} E_{inc,h} \\ E_{inc,v} \end{pmatrix} \quad 2.17$$

The amplitude scattering matrix elements S , contain all the information about the particle, such as shape, size, and refractive index. The dimensionless backscattering intensities $i(\mathbf{e}_h)$, $i(\mathbf{e}_v)$ are defined in terms of the squared modulus of the amplitude scattering matrix elements:

$$i(e_h) = |S_2|^2, i(e_v) = |S_1|^2 \quad 2.18$$

By contrast to exact scattering methods, the validity of most approximations is limited to a certain size parameter range. In principle, there is no lower size parameter limit for applying DDA. But, at the other end, as soon as the wave no longer resolves the geometric structures of the scatterer, the application of the Rayleigh approximation is desirable because of its simplicity. The program DDSCAT is used to perform the DDA to calculate the backscatter efficiency of a bullet shape particle and is described in chapter 4.

3 Experiment Setup and Reflectivity Calculations

3.1 Methodology for the Spatial and Temporal Matching

Our first priority for the comparison between instruments was to find collocated data in time and space. We found that our investigation was limited by the in-situ instrument (VIPS), because for this device there were only four days with data collected: March 5, March 9, March 12 and March 13 of 2000; their time of acquisition were 22:50:44 to 26:21:00 UTC, 18:31:59 to 22:42:00 UTC, 22:22:09 to 25:44:20 UTC and 19:21:33 to 22:29:00 UTC, respectively. As was mentioned in chapters before, the radar was nadir looking and the airplane was collecting data with various types of instruments; Figure 3.1 show a diagram of the setup of this experiment. It should be mentioned that the two instruments were not well coordinated in terms of distance between them.

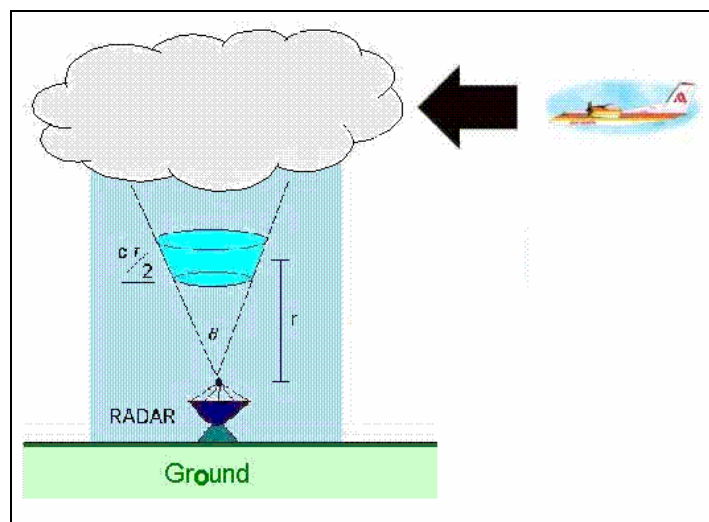


Figure 3.1 Experimental Setup of the devices used for comparison.

Given that we had VIPS data for those four days, we proceeded to examine the CPRS data to find if there were data gathered at the same times as the VIPS; but first of all we examined the parameters of the CPRS and used the beamwidth of the radar in order to find an approximate diameter of the beam at different altitudes. The diameter of the beam of the radar at a given altitude can be approximated by:

$$S = r\theta \tag{3.1}$$

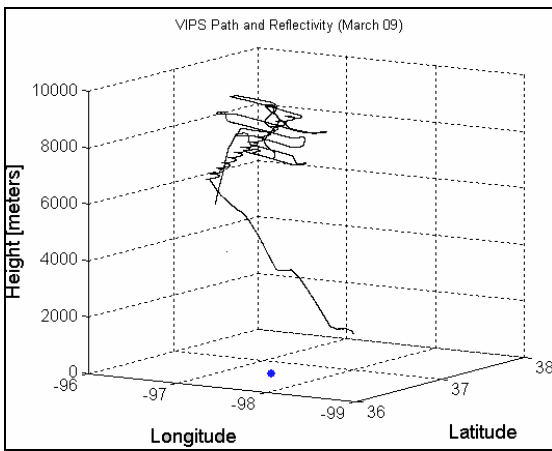
where r is altitude, and θ is radar beamwidth in radians. A table showing the approximate diameter of the radar’s beam at different altitudes is shown in table 3.1.

As was mentioned above, the two instruments were not well coordinated and for this reason only a distance of approximately 600m between instruments was the closest for the day elected for comparison. However, cirrus clouds variability is modest on scales close or smaller than 500m according to *Hogan and Illingworth, 2003*.

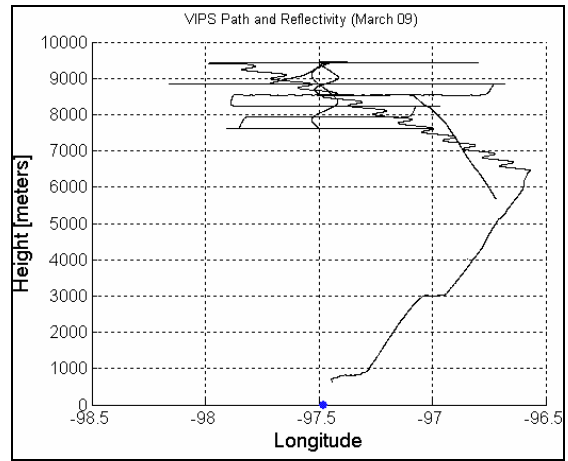
TABLE 3.1 Approximate beam diameter for several radar bands at various altitudes

Altitude [km]	Diameter of beam for: $\theta=.5^\circ$ @ 33GHz [m]	Diameter of beam for: $\theta=.18^\circ$ @ 95 GHz [m]
5,000	43.633	15.708
5,500	47.997	17.279
6,000	52.360	18.849
6,500	56.723	20.420
7,000	61.087	21.991
7,500	65.450	23.562
8,000	69.813	25.133

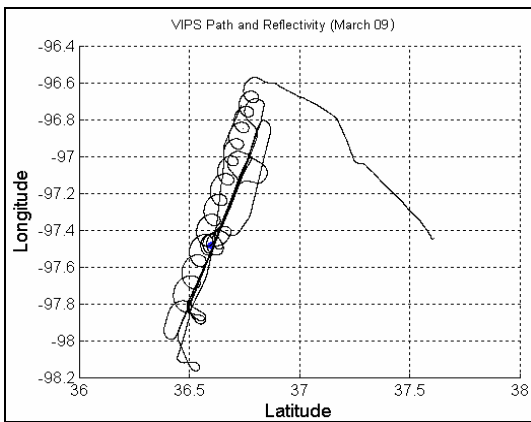
Figures 3.2, to Figure 3.4 show three views of the VIPS acquisitions points (Top, Side, and 3D view) and are placed for comparison purposes with K_a band CPRS most relevant data plots, which are for March 9, 12 and 13, respectively.



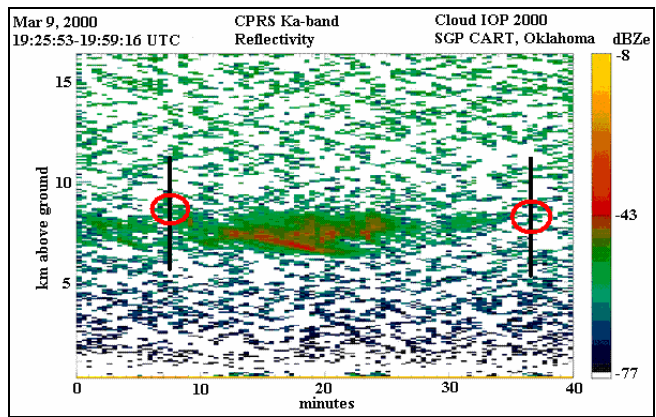
a)



b)

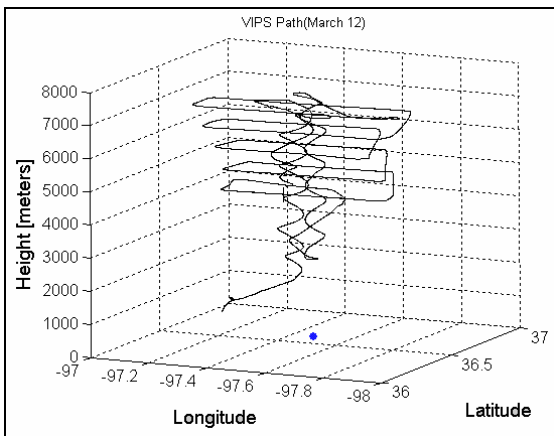


c)

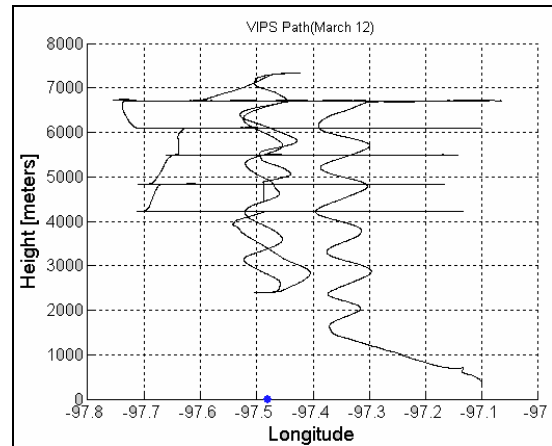


d)

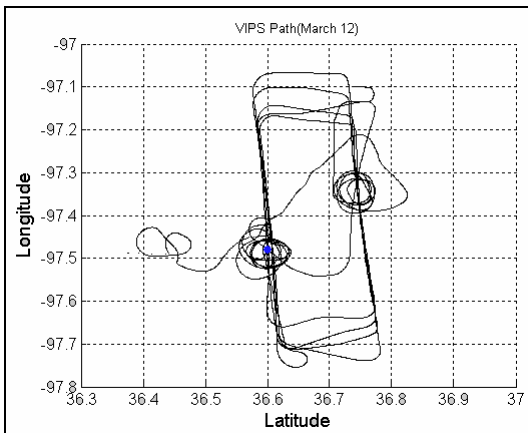
Figure 3.2 a),b) and c) are VIPS location (3D, side and top view respectively) when the instrument was gathering data from 18:31:59-22:42:00 UTC for a total of 15,000 points on March 9, 2000. d) shows CPRS 33GHz data that matched in time, but the closest points between instruments at the time of the graph above (shown by red circles) are at the beginning and end of the cloud, so this day is not a good one for comparison purposes [ARM Archive].



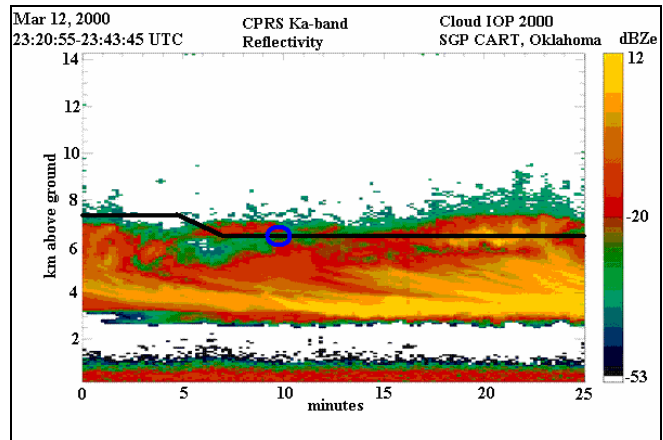
a)



b)



c)



d)

Figure 3.3 a),b) and c) are VIPS location (3D, side and top view respectively) when the instrument was gathering data from 22:22:09-25:44:20 UTC for a total of 12,132 points on March 12, 2000. d) shows CPRS 33GHz data matched in time, but the closest point between instruments at the time of the graph above (shown by a blue circle and the altitude of the plane shown by a black line) are in the cloud top region, nearly outside of the cloud, so this day is not a good one for comparison purposes [ARM Archive].

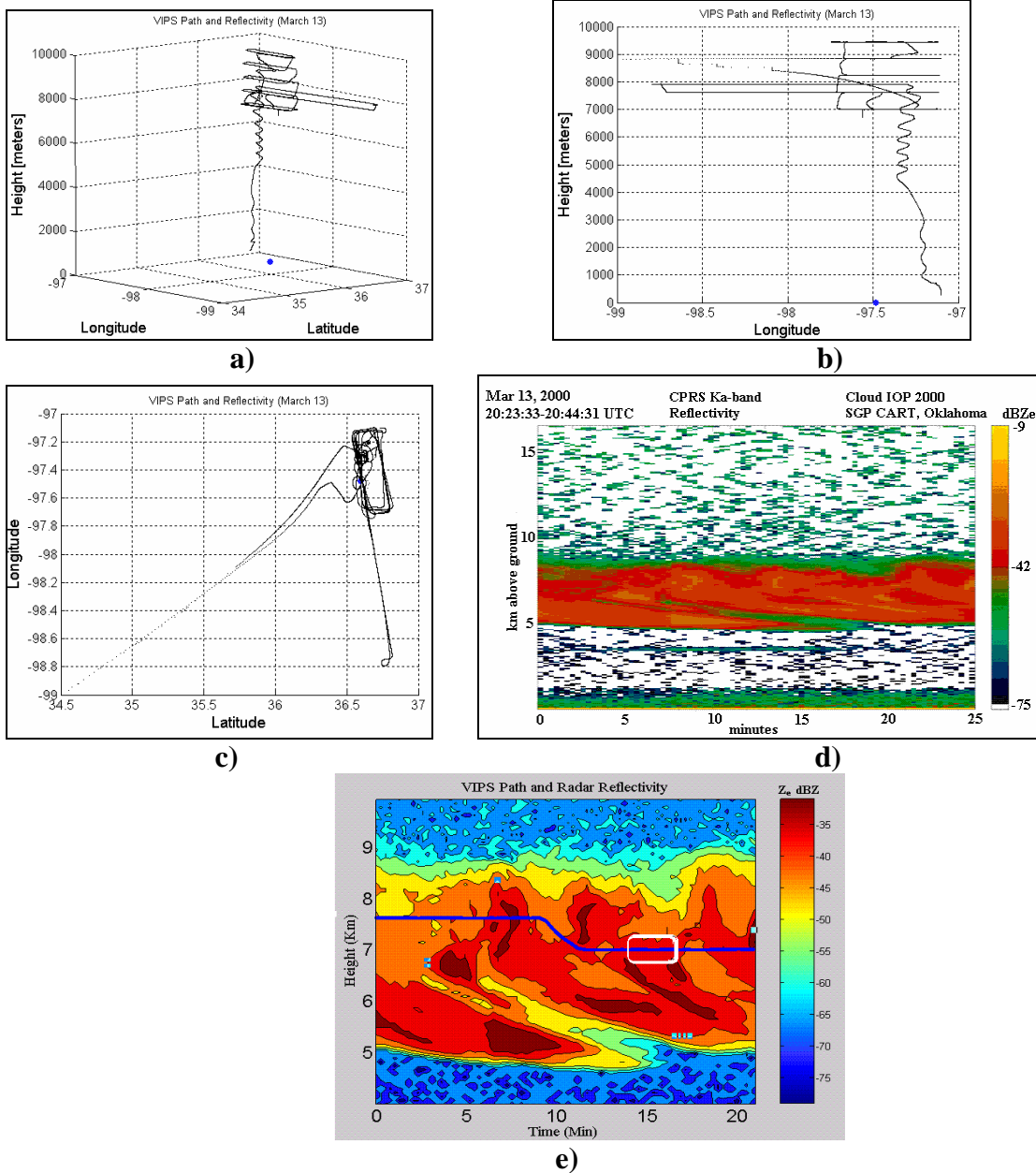


Figure 3.4 a),b) and c) are VIPS location (3D, side and top view respectively) when the instrument was gathering data from 19:21:23-22:29:00 UTC for a total of 15,711 points on March 13, 2000. d) shows CPRS 33GHz data matched in time, [ARM Archive]. e) is the same as d) but zoomed from 4 to 10 km and with a different color scale; the altitude of the plane is shown by a blue line and the closest points are inside the white rectangle lines, good matching in time and space was obtained for this day.

The distance between instruments, was obtained with the following equation [Meridian World Data, 2005]:

$$D = E * [\cos^{-1} \{ (\sin(a)) * \sin(b) + \cos(a) * \cos(b) * \cos(P_1 - P_2) \}] \quad 3.2$$

Where: E = Earth Radius=6367.3 km

a = latitude of 1st point=36.6011

b = latitude of 2nd point

P_2 =longitude of 2nd point

P_1 =longitude of 1st point = 97.4809

Now, we only had to comply with three requirements for the data in order to begin with our desired comparisons, which are: that we are looking to a cirrus cloud and that the two instruments used are close in time and space. After examining different days of the data collected, we concluded that the best day to compare both instruments was March 13, 2000. It should be mentioned that for the four days of VIPS observations, there were no data placed inside the volume of the radar beam; for the best day for comparison, March 13, 2000, the closest distance between instruments was 610 meters.

3.2 Equivalent Reflectivity Comparison

Results of the equivalent reflectivity obtained using equation 2.11 for the VIPS data for density models from *Heymsfield, B&F* and constant value, (equations 1.1-1.3), are shown on Figure 3.6 to Figure 3.11. It should be mentioned that diameters larger than 2,000 μm were not used because the VIPS didn't find any particle larger than that dimension (meaning that

$N(D > 2,000 \mu\text{m}) = 0$) within the cirrus cloud. Continuing with Figures 3.6 to 3.11, they show different perspectives of the flight track taken by the plane on March 13, 2000 from 20:36:08 to 20:38:30 UTC (closest points between CPRS and VIPS up to a maximum separation of 10 km). The colors on those figures represent the equivalent reflectivity in dBZ and are spaced in intervals of 5 dB. It should be mentioned that the scale used in Figures 3.6 and 3.7 are different from the ones used from Figures 3.8 to 3.11. Figure 3.5 shows particles distributions obtained on March 13, 2000 for our in-situ instrument (VIPS) and from a Cloud Particle Imagery (CPI); which were equipped and used at the same time during the flights (This are presented here only for comparison purposes). The relative similarity in measurements from the VIPS and CPI gives us a good indication that the data should be very reliable.

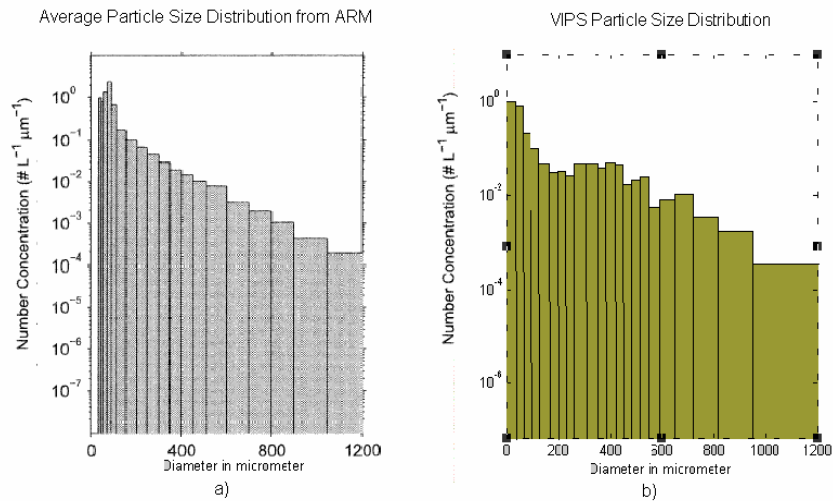


Figure 3.5 (left) Average particle size distribution from data collected between the 9 and 13 of March 2000, by the University of North Dakota Citation research aircraft, using a cloud particle imagery (CPI). (right) Particle size distribution obtained from data of the VIPS when the plane flew very close to radar location.

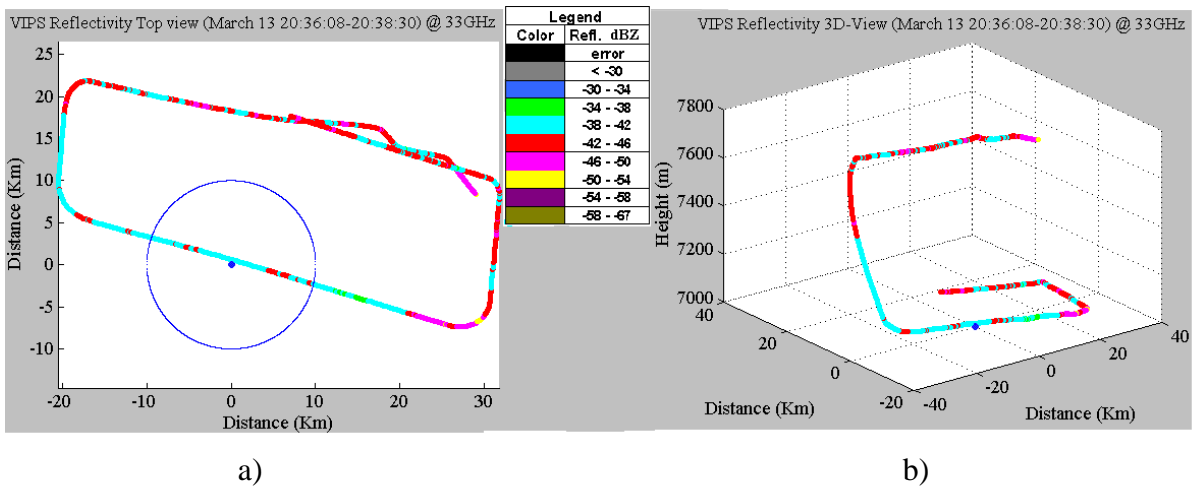


Figure 3.6 Overhead view of the VIPS flight track pattern for March 13, 2000. The blue dot at (0,0) indicates the position of the CPRS radar, the blue circle is only a reference for data that were spatially closed between sensors; while the colors represent the range of equivalent reflectivity Z_e obtained using *B&F* density equation (1.2). b) Is the same as a) but in three dimensions to show the altitude variation. (*Brown and Francis, 1995, density model at 33GHz*)

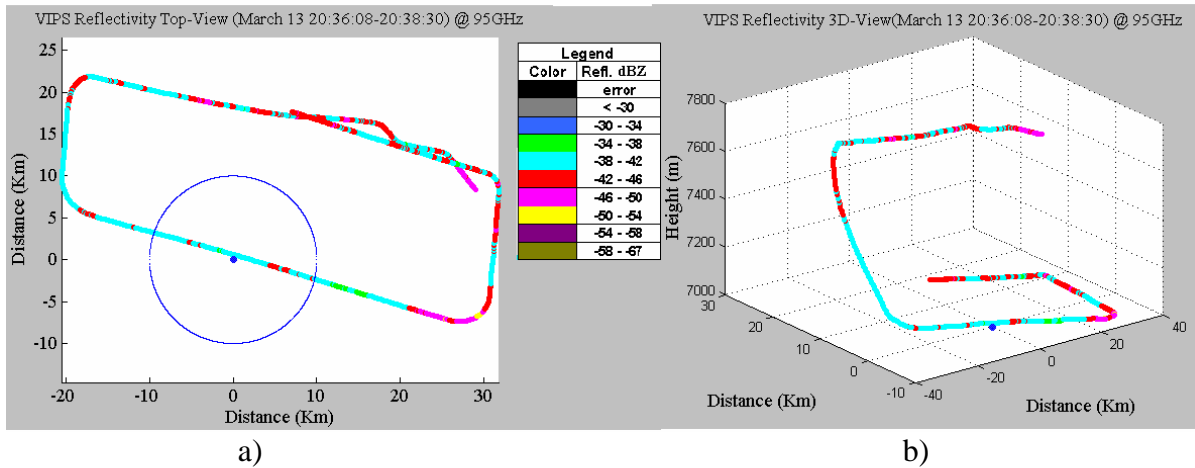
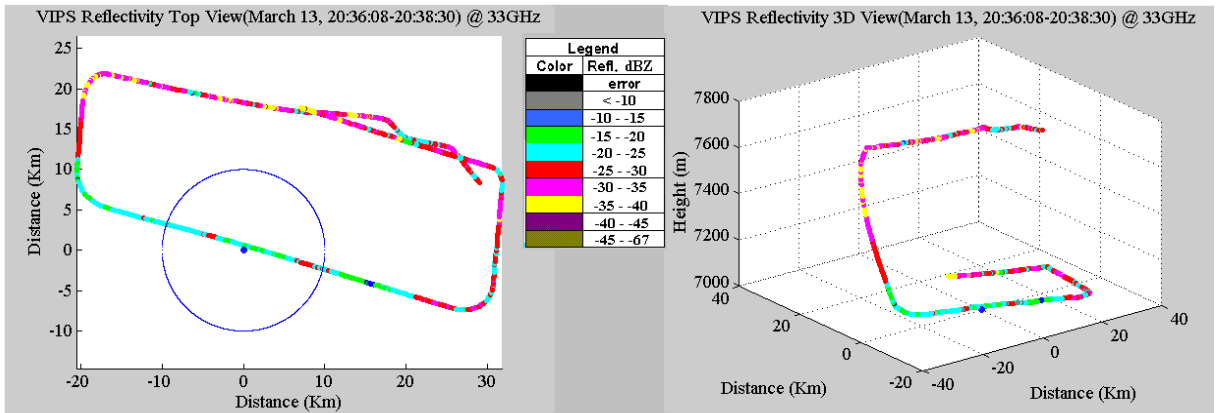


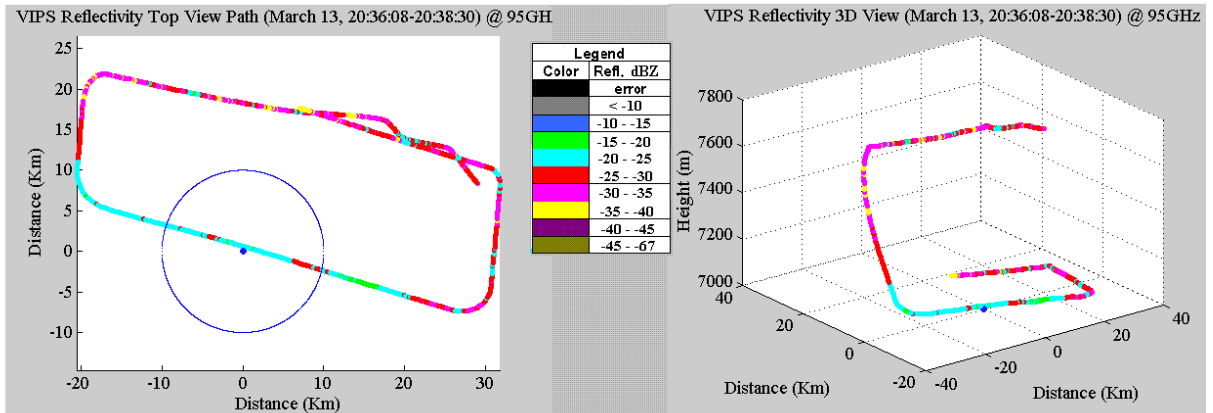
Figure 3.7 Same as Figure 3.6 but for 95 GHz.



a)

b)

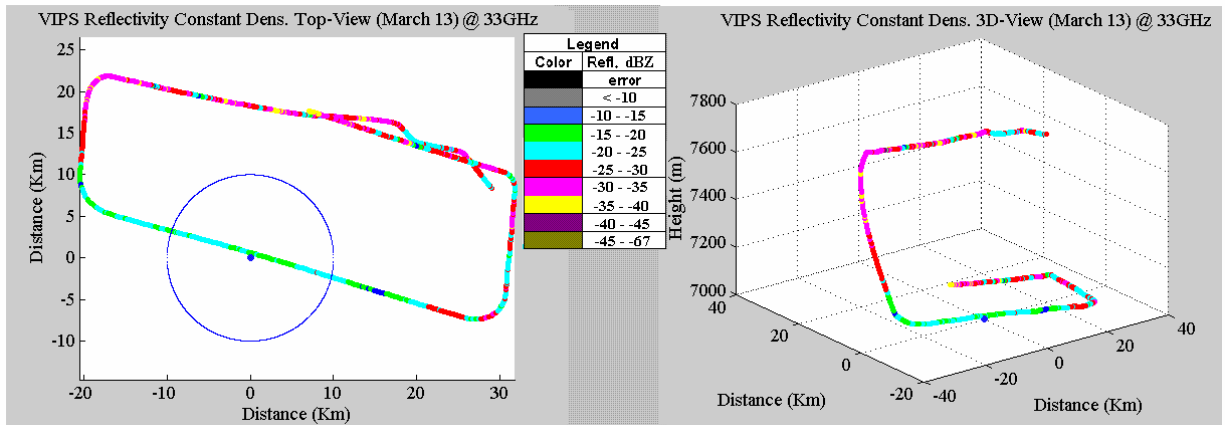
Figure 3.8 Same as Figure 3.6 but using *Heysfield et al.* density model at 33GHz.



a)

b)

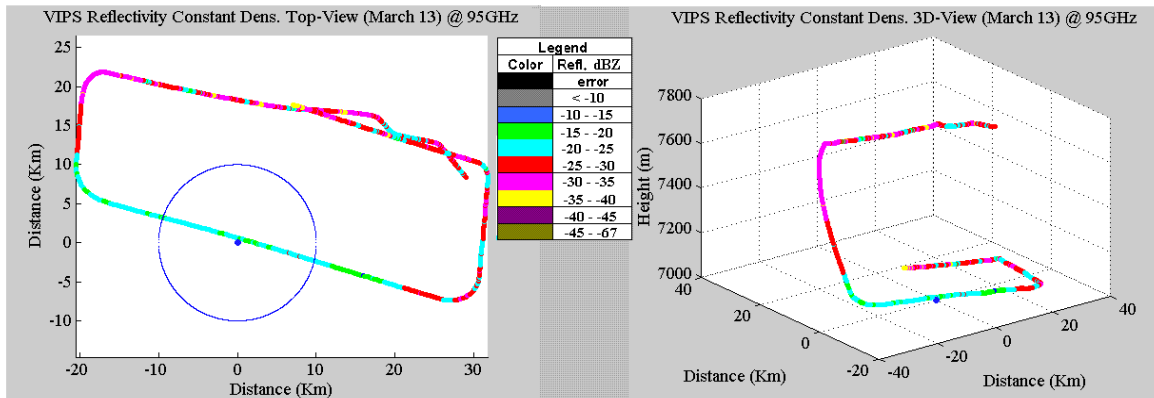
Figure 3.9 Same as Figure 3.6 but using *Heysfield et al., [1972]* density model at 95GHz.



a)

b)

Figure 3.10 Same as Figure 3.6 but using a constant ice density of 0.916 g/cm^3 at 33GHz.



a) b)
Figure 3.11 Same as Figure 3.6 but using a constant solid ice density of 0.916 g/cm^3 at 95GHz.

The equivalent reflectivity for March 13, 2000 from the CPRS as a function of time is presented in Figure 3.12, this is for the altitude at which the plane was flying at those given times (which was 7 km); for the two CPRS channels, 33 and 95 GHz.

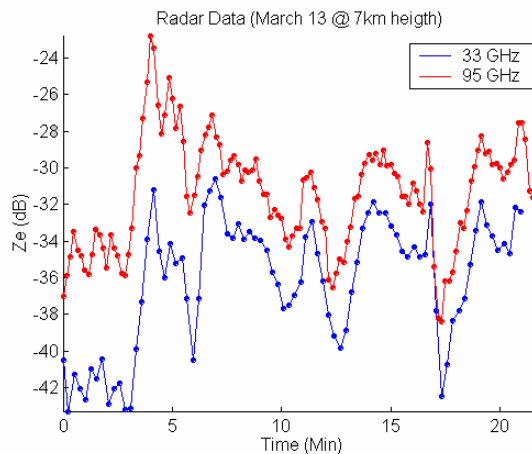


Figure 3.12 Time traces of the data showing the radar reflectivity of the two channels of CPRS data during the time when the airplane over flew over the radar, the red colored is for the 95 GHz data while the blue is for the 33 GHz data.

For the comparisons we used data from March 13, 2000 spaced up to a maximum distance of 10 km between instruments and the time of recollections were between 20:36:08

to 20:38:30 UTC. A plot showing simultaneous data from the VIPS and the CPRS measurements for 33 GHz is shown in Figure 3.13, where the CPRS data is represented by a red line and the VIPS data is represented in blue. The horizontal axis represent the time in minutes, and the green line and right vertical axis represents the distance between instruments; Z_e calculated for the VIPS in Figure 3.13 was done using equation (2.11) and using equation (1.2) density model.

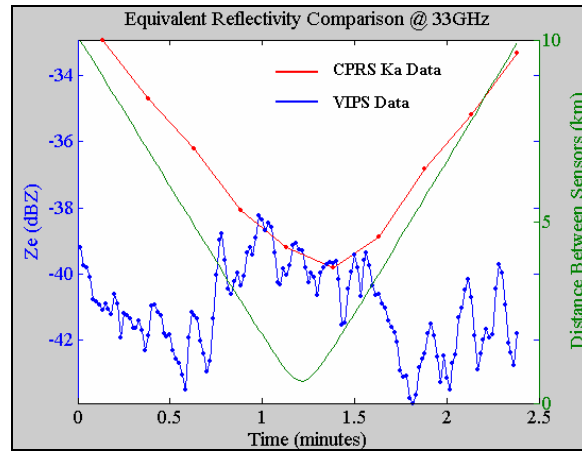


Figure 3.13 Comparison between equivalent reflectivity obtained from CPRS radar and VIPS in-situ instrument, @ 7km of height over time and distance, *Brown and Francis, 1995* density model.

Figures 3.14 and 3.15 are similar to Figure 3.13, but are obtained using *Heymsfield's* density (equation 1.1) and a constant density of 0.916 g/cm^3 , respectively. In order to obtain a meaningful quantity for the comparison between instruments, we calculated the root mean square (RMS) difference for the Z_e (equivalent reflectivity) using the following equation:

$$Z_{e_{RMS}} = \sqrt{\frac{(a_1 - b_1)^2 + (a_2 - b_2)^2 + (a_3 - b_3)^2 + \dots + (a_n - b_n)^2}{n}} \quad 3.3$$

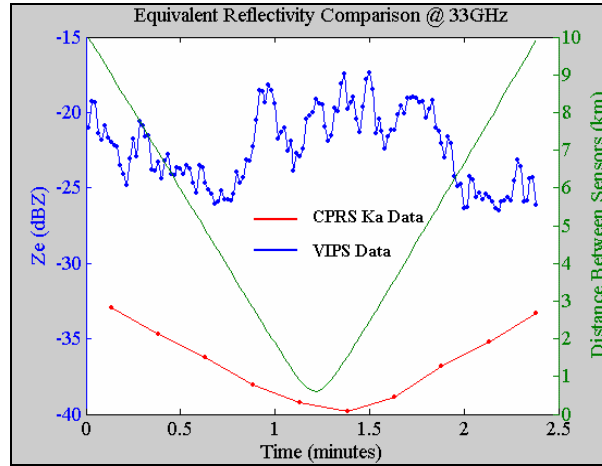


Figure 3.14 Comparison between equivalent reflectivity obtained from radar and in-situ instrument, @ 7km of height over time and distance, using *Heymsfield et al., 1972* density model.

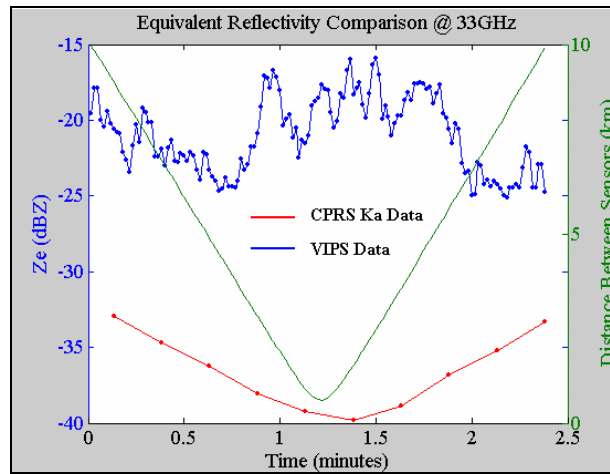


Figure 3.15 Comparison between equivalent reflectivity obtained from radar and in-situ instrument, @ 7km of height over time and distance, using a constant density of 0.916 g/cm^3 .

In order to compensate for the additional points of data from the VIPS for the comparison at 33 GHz, we used a polynomial regression of 6th degree; also because as was mentioned in section 3.1, cirrus clouds variability is modest on scales close or smaller than 500m.

$$Z_{e,radar}(t) = 3.0301t^6 - 24.067t^5 + 71.171t^4 - 95.438t^3 + 60.55t^2 - 23.311t - 30.667 \quad \mathbf{3.4}$$

where t is in seconds. Tables 3.2 to 3.3 show the RMS difference in dBZ at a separation between instruments up to 1, 5 and 10 km, for density models from *Heymsfield*, *B&F* and constant solid ice density of 0.916 g/cm^3 at a frequency of 33GHz.

TABLE 3.2 RMS Difference between instruments (*B&F* crystal density $\rho=0.07D^{-1.1}$) 33GHz.

Distance between sensors	RMS Difference
1km	0.1371 dBZ
5km	1.4593 dBZ
10km	5.3041 dBZ

TABLE 3.3 RMS Difference between instruments (*Heymsfield* density $\rho=0.78D^{-0.0038}$)33GHz.

Distance between sensors	RMS Difference
1km	5.6810 dBZ
5km	7.7267 dBZ
10km	14.8538 dBZ

TABLE 3.4 RMS Difference between instruments (constant ice density $\rho=.916 \text{ g cm}^{-3}$) 33GHz.

Distance between sensors	RMS Difference
1km	6.1116 dBZ
5km	8.4138 dBZ
10km	16.2269 dBZ

From the results shown from tables 3.2 to 3.4 (and also by looking to Figures 3.13 to 3.15) it can be appreciated that the *B&F* density model ($\rho=0.07D^{-1.1}$) gave better agreements of Z_e between instruments; also the agreement is considerably better in Table 3.2 for 1 km than in the other two tables. This results suggest that a constant density of solid ice of 0.916 g cm^{-3} cause an overestimate of Z_e ; also *Heymsfield* density model (which gives density values that don't vary a lot with respect of the dimensions of the particles) cause an overestimate of Z_e .

4 ICE CRYSTALS' SHAPE EFFECT IN RADAR MEASUREMENTS

The work presented here analyzes crystals with bullet shape, because previous studies have shown that this crystals form is the most common found in cirrus clouds [*Heymsfield and Platt*, 1984; *Mitchell and Arnott*, 1994]. The parameter of interest to observe the effect of the particles shape in equivalent reflectivity retrievals is the ξ_b (backscattering efficiency); this was done using Discrete Dipole Approximation using the software DDSCAT. The shape of the bullet was performed using *Villa et al.* code. We also used crystal density models from *Heymsfield et al.* [1972], *Brown and Francis* [1995], as well as a constant density to obtain the refraction indices necessary to estimate the backscattering efficiencies using DDSCAT.

4.1 Simulation of Bullet Shape

4.1.1 DDSCAT Program and Bullet Shape Parameters

As was mentioned in previous chapters, we used the DDSCAT software to compute the backscattering produced by one ice crystal's bullet particle. This program is based on the discrete-dipole approximation method, DDA. The software include some common geometric shapes such as hexagonal plates, prisms, cylinders and others, but offer the possibility to create even more complex shapes, and we proceeded to take advantage of the *Villa et al.* code used to simulate bullet particles. The DDA method approximates the object's geometry by means of a polarizable dipoles array; DDSCAT distributes these dipoles on a cubic lattice as was shown in Figure 1.2.

Even though DDA can describe any geometry, it is limited by a minimum distance d that should exist between dipoles. This distance is inversely proportional to any structural longitude on the target and to the wavelength. Previous studies [Draine and Flatau, 1994] sum up the two criteria in equation 4.1.

$$|m|kd < 0.5 \quad 4.1$$

with m as the complex refractive index of the object material, and k as the wavenumber of the surrounding medium.

Another factor that should be considered is the number of dipoles that describe the target. For each dipole an electric field is calculated, and at the end the summation of all the fields due to each dipole is the total electric field, from which the backscattering coefficient is computed and other products as the absorption and scattering coefficient factors. In order to obtain more accurate results, the number of dipoles used for a simulation should be considerably large.

The construction of the bullet in Villa et al. code was done using the following relations: each bullet has a longitude relation [Heymsfield and Knollenberg, 1972], L (mm), versus width, w (mm), (twice times the apothem (define)) for temperatures between -18° and -20°C (see Figure 4.1) given by:

$$w = 0.25L^{0.7856} \quad (\text{mm}), \quad 4.2$$

for bullets with $L \leq 0.3$ mm, and

$$w = 0.185L^{0.532} \quad (\text{mm}), \quad 4.3$$

for bullets with $L \geq 0.3$ mm.

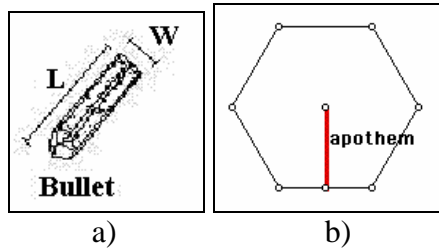


Figure 4.1 Schematics to describe the dimensions in a cirrus cloud bullet shaped particle. a) Bullet side view. b) Cross section of a bullet.

Now the inputs to DDSCAT are performed using a file named `ddscat.par` and the methodology is presented in Figure 4.2., the inputs are shape (bullet), particle's size (D_m from the VIPS), number of dipoles (15,692 dipoles, which is sufficiently large to yield accurate results at the frequencies of interest), wavelength (9.0909mm for 33GHz and 3.1579mm for 95GHz), refraction index (which is obtained using *Heymsfield, Brown and Francis* density models and constant density), and the target orientation (which would be explained in more detail the next paragraph).

In DDSCAT the target is oriented using what it's called the "Lab Frame" which is shown in Figure 4.3. The incident radiation is defined to propagate in the $+x$ direction; and the inputs in DDSCAT for the target orientation are the following three angles: Θ , Φ , and β . Θ is the angle between \hat{a}_1 and \hat{x} . The angle Φ refers to the rotation of \hat{a}_1 around \hat{x} , while β introduces an additional rotation of \hat{a}_2 around \hat{a}_1 . The ranges of these angles are: $0^\circ < \Theta < 180^\circ$, and $0^\circ < \beta, \Phi < 360^\circ$.

Due to the randomness of the particles in both shape (bullet is said to be the most predominant shape, but not the only present) and orientation, we calculate averaging over

random orientations in DDSCAT in the following manner: we let DDSCAT run β from 0° to 360° , Φ from 0° to 360° and we let Θ run from -30° to 30° .

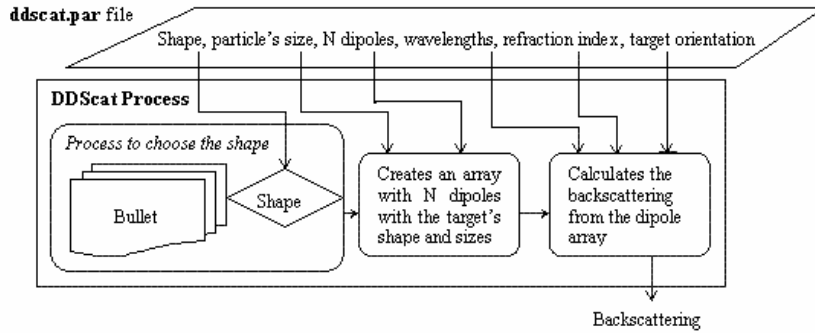


Figure 4.2 Methodology used to create a bullet formed by an array of N dipoles. (General process)

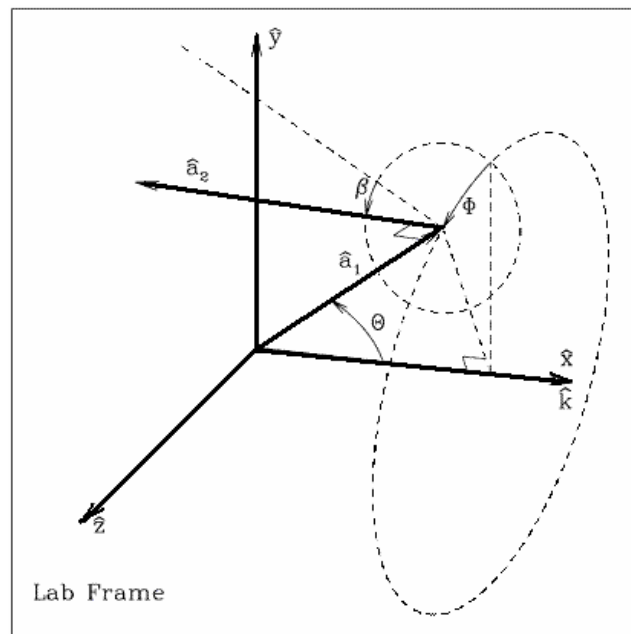


Figure 4.3 Target orientation in equation in the Lab Frame. \hat{x} is the direction of propagation of the incident radiation, and the \hat{y} is the direction of the “real” component of the first incident polarization mode. In this coordinate system, the orientation of target axis \hat{a}_1 is specified by angles Θ and Φ . With target axis \hat{a}_1 fixed, the orientation of target axis \hat{a}_2 is then determined by angle β specifying rotation of the target around \hat{a}_1 . When $\beta=0$, \hat{a}_2 lies in the \hat{a}_1 , \hat{x} plane.

4.1.2 *Bullet Backscattering vs Mie Backscattering comparison*

Figure 4.4 to 4.9 shows backscattering efficiencies obtained using DDSCAT and compared with Mie results, for the three density models at 33 and 95 GHz. It can be seen that at 33 GHz the difference between Mie and bullet DDA simulated backscattering obtained for all the three density models is completely negligible, in the three cases they were just slightly lower (the effect of these backscattering can be seen on Figures 4.10 to 4.12). However, as was expected, significant differences appear when looking the backscattering efficiencies at 95 GHz. For the *Brown and Francis* density model the bullet simulated backscattering was significantly bigger than the Mie backscattering for the larger radius taken into account (radius up to $1,120\mu$ or diameter of $2,240\mu\text{m}$); also of special notice was that the oscillatory behavior was not present or visible for the radius simulated (the oscillatory behavior can be seen if larger radius are use).

On the other hand the oscillatory behavior can be clearly seen (due to the wavelength been comparable to the crystal's sizes at 95 GHz) for the *Heymsfield* density model, and for a constant density of 0.916 g/m^3 at a frequency of 95 GHz. Their backscattering efficiency results are significantly lower for the *B&F* density model at 95 GHz, Mie backscattering underestimate the backscattering obtained from a bullet particle, meanwhile when using the density of solid ice or the *Heymsfield* density model, Mie overestimate the backscattering obtained for a bullet particle.

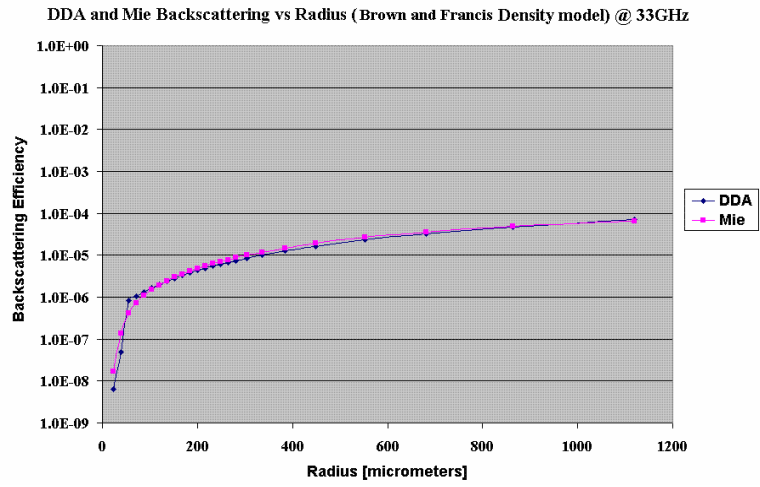


Figure 4.4 Backscattering comparison using *Brown and Francis* crystal density @ 33GHz.

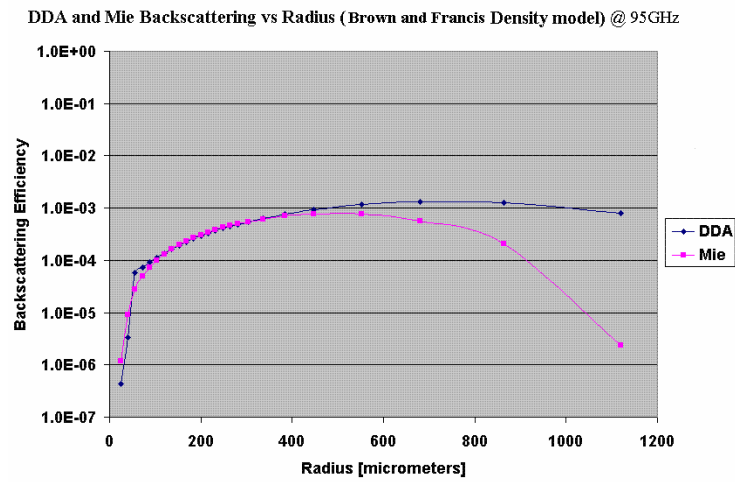


Figure 4.5 Backscattering comparison using *B&F* density @ 95GHz.

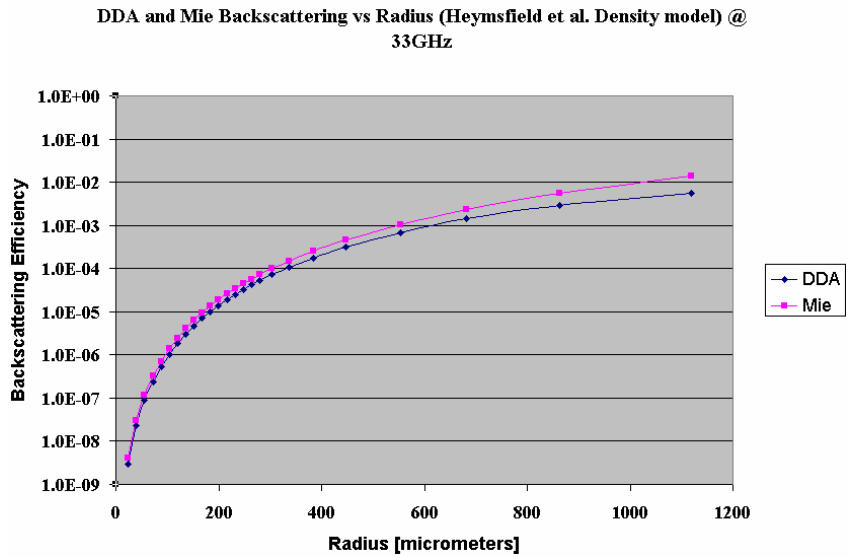


Figure 4.6 Backscattering comparison using *Heymtsfield* density model @ 33GHz.

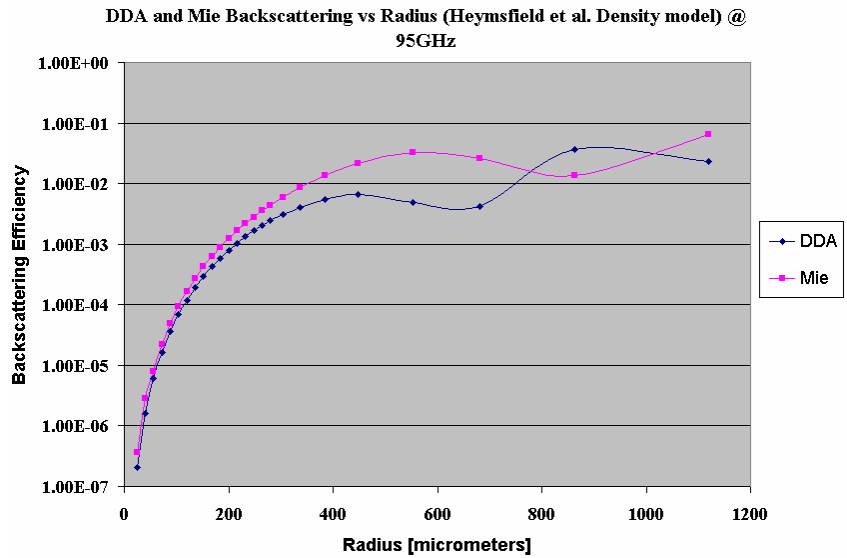


Figure 4.7 Backscattering comparison using *Heymtsfield* crystal density @ 95GHz.

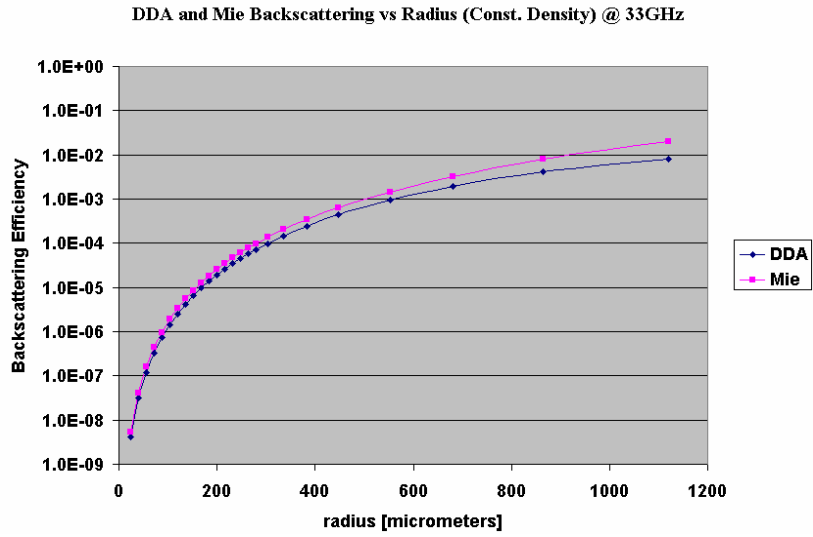


Figure 4.8 Backscattering comparison using constant solid ice density @ 33GHz.

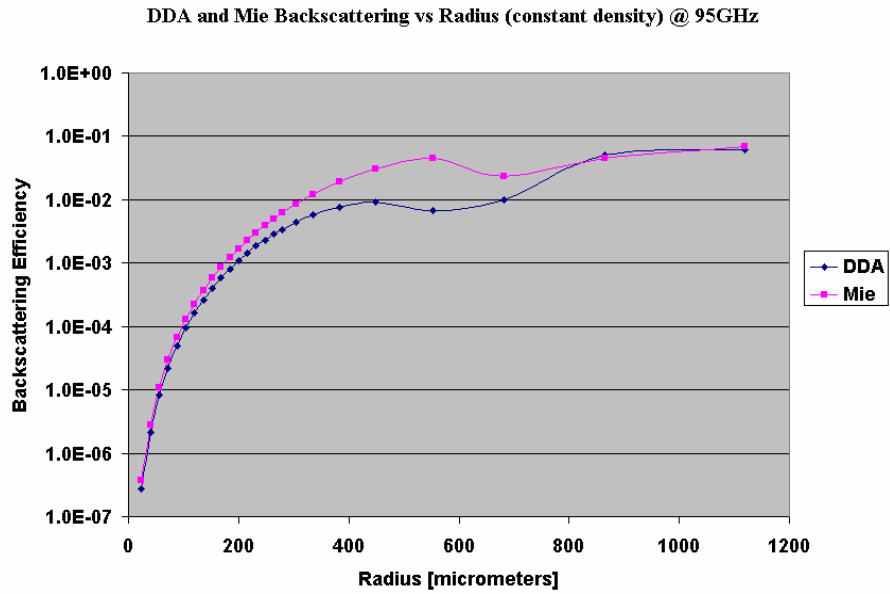


Figure 4.9 Backscattering comparison using constant solid ice density @ 95GHz.

4.2 Equivalent Reflectivity from VIPS Bullet Simulated Particles

Equivalent reflectivity results and comparisons as the one presented in section 3.3 are shown for the bullet shaped ice particles from Figure 4.10 to Figure 4.12. From these figures we can conclude that there is not a significant difference in Z_e between Mie and bullet simulated particles at 33 GHz for the different density models. But at 95 GHz the results using the bullet simulated backscattering resulted in better agreement with the CPRS data, than the Mie solution. The agreement can be better appreciated when using the *Brown and Francis* density model applied to VIPS (Figure 4.10 b); also better agreements occurs where airplane is closer (horizontally) to the ground radar.

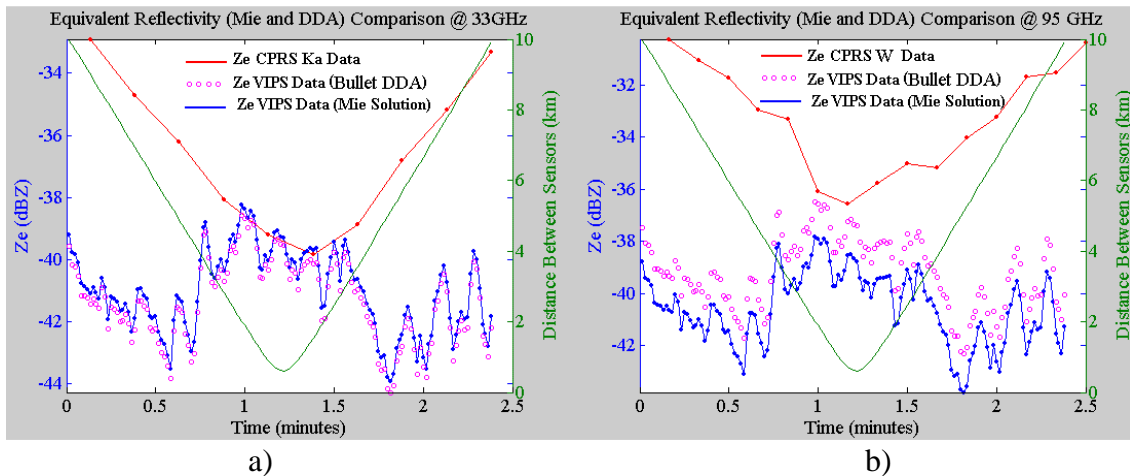


Figure 4.10 a) Comparison between equivalent reflectivity obtained from radar and in-situ instrument, @ 7km of height over time and distance, using a variable density (*Brown and Francis*) of $\rho=0.07D^{-1.1}$ using backscatter simulated using DDSCAT bullet model (purple circles). b) is the same as a) but at 95 GHz.

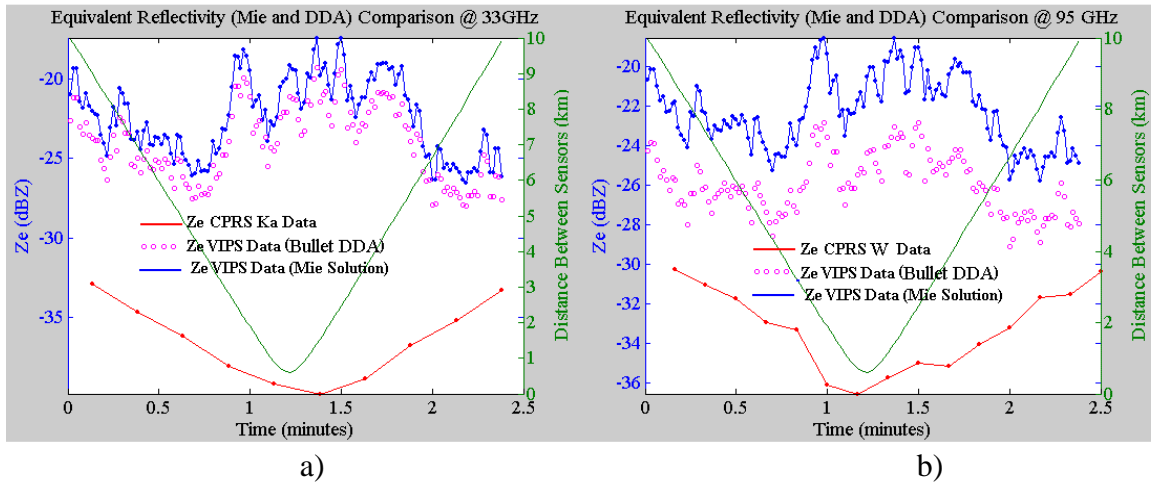


Figure 4.11 a) Comparison between equivalent reflectivity obtained from radar and in-situ instrument, @ 7km of height over time and distance, with a variable density of $\rho=0.78D^{-0.0038}$ (Heymsfield *et al.*) using backscatter simulated using DDSCAT bullet model (purple circles). b) is the same as a) but at 95 GHz.

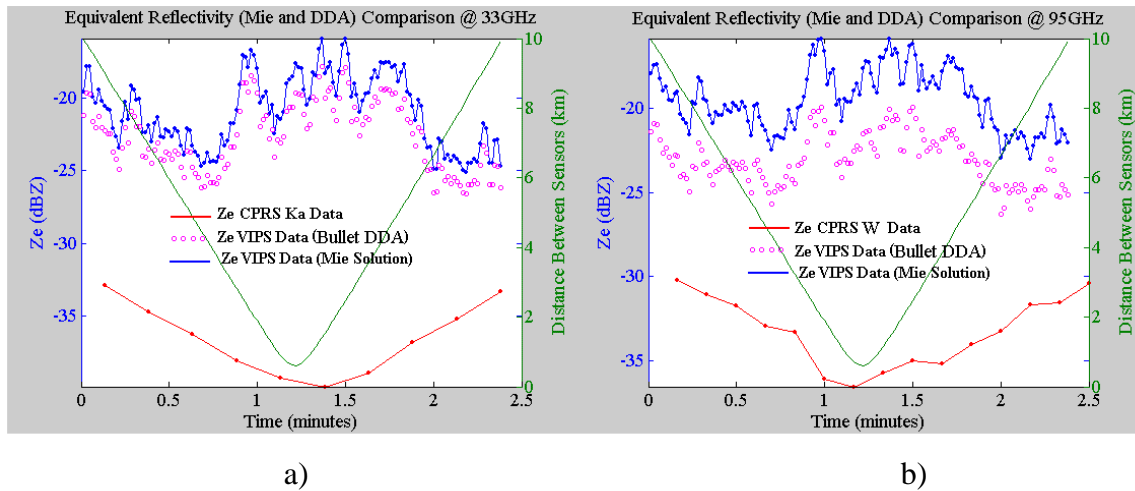


Figure 4.12 a) Comparison between equivalent reflectivity obtained from radar and in-situ instrument, @ 7km of height over time and distance, using a constant density of $\rho=0.916$ using backscatter simulated using DDSCAT bullet model (purple circles). b) is the same as a) but at 95 GHz.

5 ICE WATER CONTENT (*IWC*) RETRIEVAL

IWC is an important cloud microphysical parameter determining cloud radiative properties. Various relationships between *IWC* and radar reflectivity, summarized by *Sassen* [1987], have been reported; however there is large spread in values among these relationships and research to improve them is ongoing.

5.1 *IWC* derivation for the VIPS data

Now that the reflectivity analysis and comparison is completed we proceed to develop an *IWC* model for the VIPS data of the form:

$$IWC = aZ_e^b \quad [\text{g/m}^3] \quad 5.1$$

this should be accomplished by computing the discrete values of *IWC* using the following obvious equation [*Sekelsky*, 1999]:

$$IWC = 0.001 \int_0^{\infty} N(D) \rho(D) \left(\frac{4}{3}\right) \pi \left(\frac{D}{2}\right)^3 dD \quad [\text{g/m}^3] \quad 5.2$$

where $N(D)$ is the particle size distribution (PSD) in $(\text{mm}^{-1}\text{m}^{-3})$, D is in (mm) and $\rho(D)$ and *IWC* are in (g/m^3) .

Because *IWC* is also dependent of the density (like Z_e), we applied *Heymsfield* et al. and *Brown and Francis* crystal density models (Equations 1.1 and 1.2) as well as constant density. For every value of Z_e we associated a value of *IWC* and then, using logarithmic regression, we obtained the coefficients a and b to create an *IWC* model of the form of equation 5.1.

Tables 5.1 shows the coefficients obtained to create the *IWC* models for the density of interest in this investigation at K_a band. The results of *IWC* as a function of Z_e using different density models at K_a band and compared to the *IWC* models equations 1.3 to 1.6, are shown from Figure 5.1 to 5.3; were the *IWC*- Z_e relationships obtained from the different density models is shown in magenta color.

TABLE 5.1 Coefficients a and b for the new calibrated crystal density models at 33GHz

Ice Crystal Density Model	Coefficient a	Coefficient b
<i>Brown and Francis</i>	0.8735	0.9543
<i>Heymsfield et al.</i>	0.003680	0.3720
solid ice density 0.916 g/m ³	0.003819	0.3715

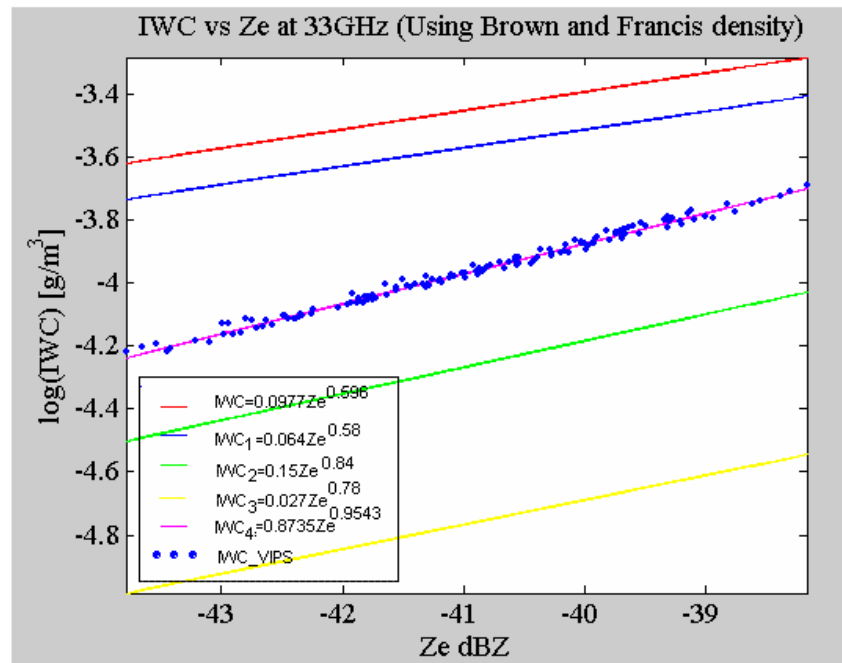


Figure 5.1 Various *IWC* models applied to the in-situ data using *B&F* ice crystal density ($\rho(D)=0.07D^{-1.1}$).

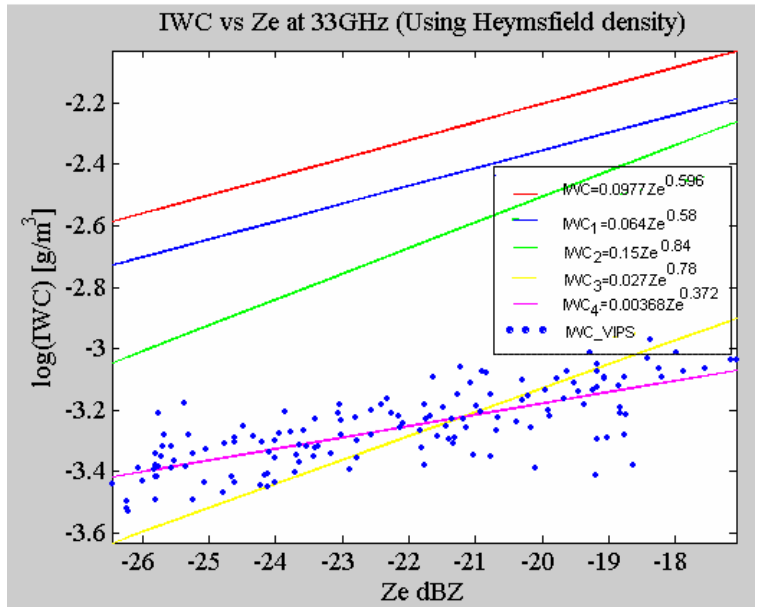


Figure 5.2 Various IWC models applied to the in-situ data using *Heymsfield* et al. ice crystal density ($\rho(D)=0.78D^{-0.0038}$). The blue dots represent the IWC obtained for the VIPS data.

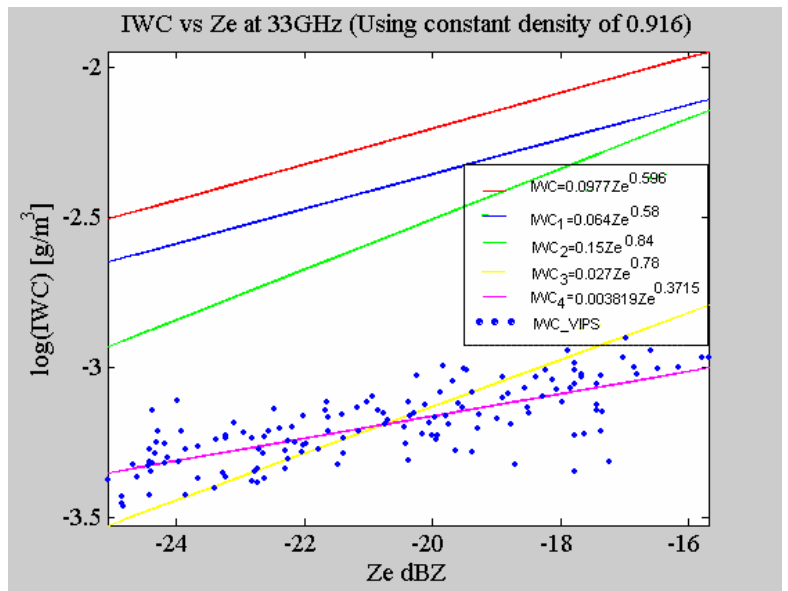


Figure 5.3 Various IWC models applied to the in-situ data using a constant density $\rho=0.916 \text{ g/m}^3$.

To examine the difference between the various *IWC* models with respect to the in-situ data we applied the RMS equation 3.3 for the different ice crystal density models and the results are shown from table 5.2 to 5.4. Given the results for the *IWC* using *Brown and Francis* density at 33 GHz, it can be seen that the discrete values are close to the *IWC*- Z_e relationship obtained for it of $IWC_4 = 0.8735Z_e^{0.9543}$ (which is the new calibrated model recommended in this work) and as was expected, the second relation closer to it was equation 1.6, which also used the *Brown and Francis* density. Meanwhile, when using *Heymsfield et al.* and solid ice densities, their results were very similar (their *IWC*- Z_e relationships coefficients were similar), their variability was high in comparison to the relationships obtained for them $IWC_4 = 0.003680Z_e^{0.3720}$, $IWC_4 = 0.003819Z_e^{0.3715}$, respectively.

TABLE 5.2 RMS results for the *IWC* models using *B&F* density model at 33GHz

IWC model (equation)	RMS Difference
IWC (1.4)	0.5174
IWC_1 (1.5)	0.4001
IWC_2 (1.6)	0.2979
IWC_3 (1.7)	0.7968
IWC_4	0.0123

TABLE 5.3 RMS results for the *IWC* models using *Heymsfield* density model at 33GHz

IWC model (equation)	RMS Difference
IWC (1.4)	0.9316
IWC_1 (1.5)	0.7841
IWC_2 (1.6)	0.5879
IWC_3 (1.7)	0.1374
IWC_4	0.0821

TABLE 5.4 RMS results for the *IWC* models using constant density at 33GHz

IWC model (equation)	RMS Difference
IWC (1.4)	0.9455
IWC_1 (1.5)	0.7959
IWC_2 (1.6)	0.6346
IWC_3 (1.7)	0.1314
IWC_4	0.0821

6 CONCLUSIONS AND FUTURE WORK

Data from cirrus clouds on March 13 of 2000 from the CPRS and VIPS were found which matched satisfactorily in time and space. The equivalent reflectivity obtained from both instruments compare favorably when both instruments were close in time and space and when the *Brown and Francis* [1995] density was applied, also their RMS values were smaller when the points compared were closer (See Fig. 3.13). It was found that the effect of the ice particles shape was negligible at 33 GHz, but at 95 GHz the effect causes significant changes. By taking the shape effect into account at 95 GHz, there was better agreements between radar's and the VIPS's Z_e for all the densities used.

IWC - Z_e relationships for the three densities used in this investigation were obtained at 33 GHz, the relationship obtained using the *B&F* density, resulted the most reliable (the shape, and the low variability in the discrete values); i.e. $IWC_4 = 0.8735Z_e^{0.9543}$, which is the new calibrated model recommended in this work. Meanwhile, when using *Heymsfield* and solid ice densities, the results were very similar (their IWC - Z_e relationships coefficients were similar), and the variability was higher compared with relationships obtained for $IWC_4 = 0.003680Z_e^{0.3720}$, $IWC_4 = 0.003819Z_e^{0.3715}$, respectively.

As part of future work it is desirable to make comparisons between the two CPRS channels, but with the VIPS data. In addition, the particle size distribution from the radar data could be retrieved to compare it with the VIPS data.

REFERENCES

Absolute Astronomy, http://www.absoluteastronomy.com/encyclopedia/c/ci/cirrus_cloud.htm. 2005.

ARM Archive, <http://www.archive.arm.gov/>

Aydin, K. and C. Tang, "Millimeter wave radar scattering from model ice crystal distributions," *IEEE Trans. Geosci. Remote Sens.*, vol. 35, pp. 140-146, 1997 a.

Aydin, K. and C. Tang, "Relationship between IWC and polarimetric radar measurement at 94 and 220 GHz for hexagonal columns and plates," *J. Atmos. Ocean. Technol.*, vol. 14, pp. 1055-1063, 1997 b.

Aydin, K., and T. M. Walsh, "Computational study of millimeter wave scattering from bullet rosette type ice crystal," Int. Geoscience and Remote Sensing Symp., Lincoln, NE, IEEE, 563-565, 1996.

Aydin, K., and T. M. Walsh, "Millimeter wave scattering from spatial and planar bullet rosettes," *IEEE. Trans. Geosci. Remote. Sens.*, 37, pp. 1138-1150, 1999.

Brown, P. R. A., and P. N. Francis "Improved measurements of the ice water content in cirrus using a total-water probe," *J. Atmos. Ocean. Technol.*, 12, pp. 410-414, 1995.

Clothiaux, E.E., M. A. Miller, B. A. Albrecht, T. P. Ackerman, J. Verlinde, D. M. Babb, R. M. Peters and W. J. Syrett, "An evaluation of a 94 GHz radar for remote sensing of cloud properties," *J. Atmos. Ocean. Technol.*, 12, no. 2, pp. 201-229, 1995.

Draine, B. T., and P. J. Flatau, "User Guide to the discrete dipole approximation code DDSCAT version 5a," Princeton Observatory Preprint POPE-695, Princeton University Observatory, Princeton University, Princeton, NJ, 39 pp. [Available from Princeton University Observatory, Princeton University, Princeton, NJ 08544-1001; available via anonymous ftp from astro.princeton.edu/draine/scat/ddscat/ver5a.], 2001.

Dungey, C. E. and C. F. Bohren, "Backscattering by nonspherical hydrometeors as calculated by the coupled-dipole method: An application in radar meteorology," *J. Atmos. Ocean. Technol.*, vol. 10, pp. 526-532, 1993.

- El-Magd, A., V. Chandrasekar, V. Bringi, W. Strapp, "Multiparameter Radar and in situ Aircraft Observation of Graupel and Hail," *IEEE Transactions on geoscience and remote sensing* , vol. 38, no.1 January 2000.
- Evans, F., "Remote Sensing Seminar: Submillimeter Rem. Sens. Of Clouds, U. Colorado". <http://nit.colorado.edu/mwcirrus/remsentalk/slide0.html>. 2001.
- Evans, K, and J. Vivekanandan, "Multiparameter Radar and Microwave Radiative Transfer Modeling of Nonspherical Atmospheric Ice Particles," *IEEE Transactions on Geoscience and Remote Sensing* , vol. 28, no.4 July 1990.
- Galloway, J., A. Pazmany, J. Mead, R. E. McIntosh, D. Leon, J. French, R. Kelly, and G. Vali, "Detection of ice hydrometeor alignment using airborne W-band polarimetric radar," *J. Atmos. Oceanic Technol.*, Vol.14, 3-12, 1997.
- Heymsfield, A. J. and R. G. Knollenberg, "Properties of cirrus generating cells," *J. Atmos. Sci.*, vol. 29, pp. 1358-1366, 1972.
- Heymsfield, A., and C. M. R. Platt, "A parameterization of the particle size spectrum of ice clouds in terms of the ambient temperature and the ice water content," *J. Atmos. Sci.*, Vol.41, 846-855, 1984.
- Heymsfield, A., http://www.atd.ucar.edu/dir_off/airborne/visp.html 2000.
- Heymsfield, A., C. Schmitt, A. Bansemer, D. Baumgardner, E. Weinstock, J. Smith, and D. Sayres, "Effective Ice Particle Densities for Cold Anvil Cirrus", *Geophysical Research Letters*, Vol.31, 2004.
- Hogan, R. J., and A. J. Illingworth. "Parameterizing ice cloud inhomogeneity and the overlap of inhomogeneities using cloud radar data". *J. Atmos. Sci.*, Vol.60, pp.756-767, 2003.
- Hogan, R. J., M. P. Mittermaier, and A. J. Illingworth. "The retrieval of ice water content from radar reflectivity factor and temperature and its use in evaluating a mesoscale model", *J. Appl. Meteorol.*, September 2004.
- Lemke, H., M. Quante, O. Danne, E. Raschke, "Backscattering of radar waves by non-spherical atmospheric ice crystals: An application of the discrete dipole approximation". 1998.

Liu, C. and A. Illingworth, "Toward more accurate retrievals of Ice Water Content from Radar Measurements of Clouds," *Journal of Applied Meteorology*, Vol.39, 1999.

Metcalf, J. I., "Radar observations of changing orientations of hydrometeors in thunderstorms," *Journal of Applied Meteorology*, Vol.34, 757-772, 1995.

Meridian World Data, <http://www.meridianworlddata.com/Distance-Calculation.asp>. 2005.

Schmidt, E. O., D. P. Kratz and B. A. Wielicki, "Effects of cirrus clouds and the atmosphere over land and ocean surfaces," *Proceedings of IGARSS 93 IEEE*, vol. 3, pp. 1107-1112, 1993.

Sekelsky, S. M. , and R. E. McIntosh, "Cloud Observations with a Polarimetric 33 GHz and 95 GHz radar". *Meteor. Atmos. Phys.*, Vol. 58, pp. 123-140, 1996.

Sekelsky, S. M., W. L. Ecklund, J. M. Firda, K. S. Gage, R. E. McIntosh, "Particle Size Estimation in Ice-Phase Clouds Using Multifrequency Radar Reflectivity Measurements at 95, 33 and 2.8 GHz," *J. Appl. Meteor.*, 38, pp. 5-27, 1999.

Simpson, J., C. Kummerow, W.-K. Tao, and R. F. Adler, "On the Tropical Rainfall Measuring Mission (TRMM)," *Meteor. Atmos. Phys.*, vol. 60, pp. 19-36, 1996.

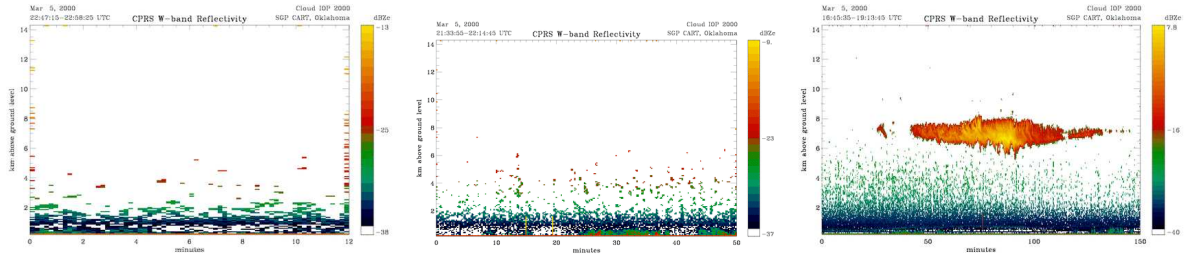
Tang, C. and K. Aydin, "Scattering from ice at 94 and 220 GHz millimeter wave frequencies," *IEEE Trans. Geosci. Remote Sens.*, vol. 33, pp. 93-99, 1995.

Ulaby, F. T., Moore R. K., Fung A. K., *Microwave Remote Sensing*, Addison Wesley, Volume 1, Chapter 5, 1986.

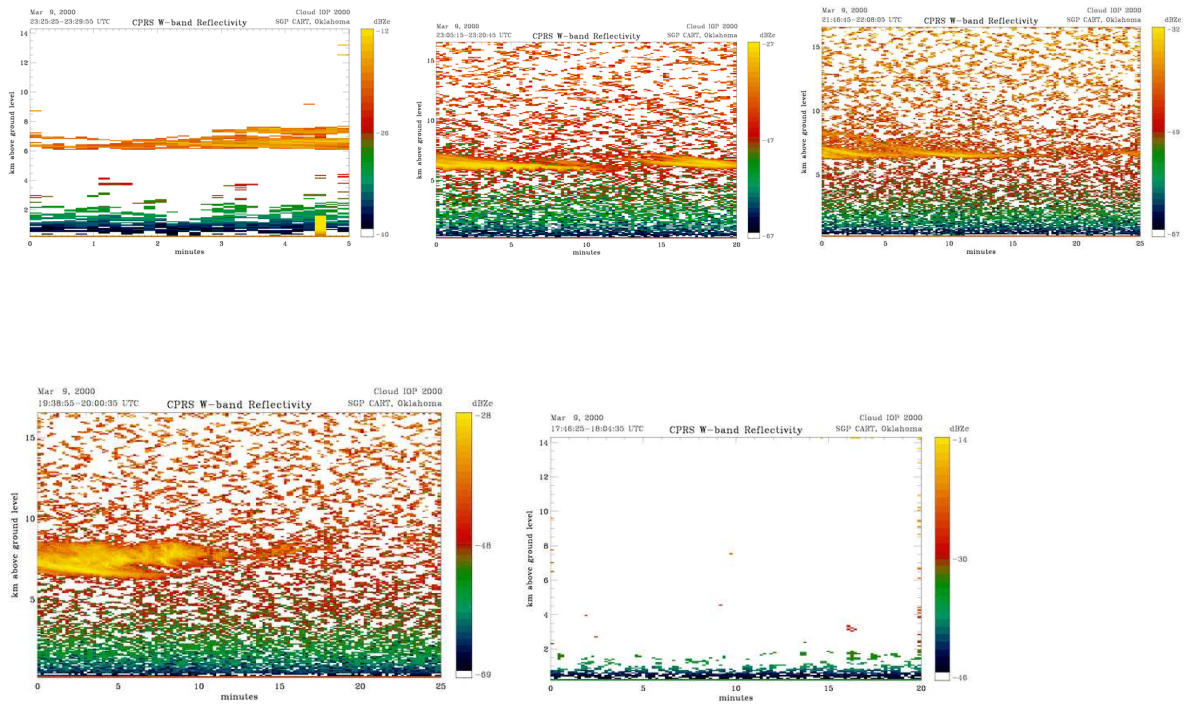
Villa, J., S.L. Cruz-Pol, and S.M. Sekelsky, "Modeling, Simulation and Comparison Study of Cirrus Clouds Ice Crystals," *SPIE 9th International Symposium on Remote Sensing*, Crete, Greece, 2002.

APPENDIX A. CPRS 95GHZ GRAPHS

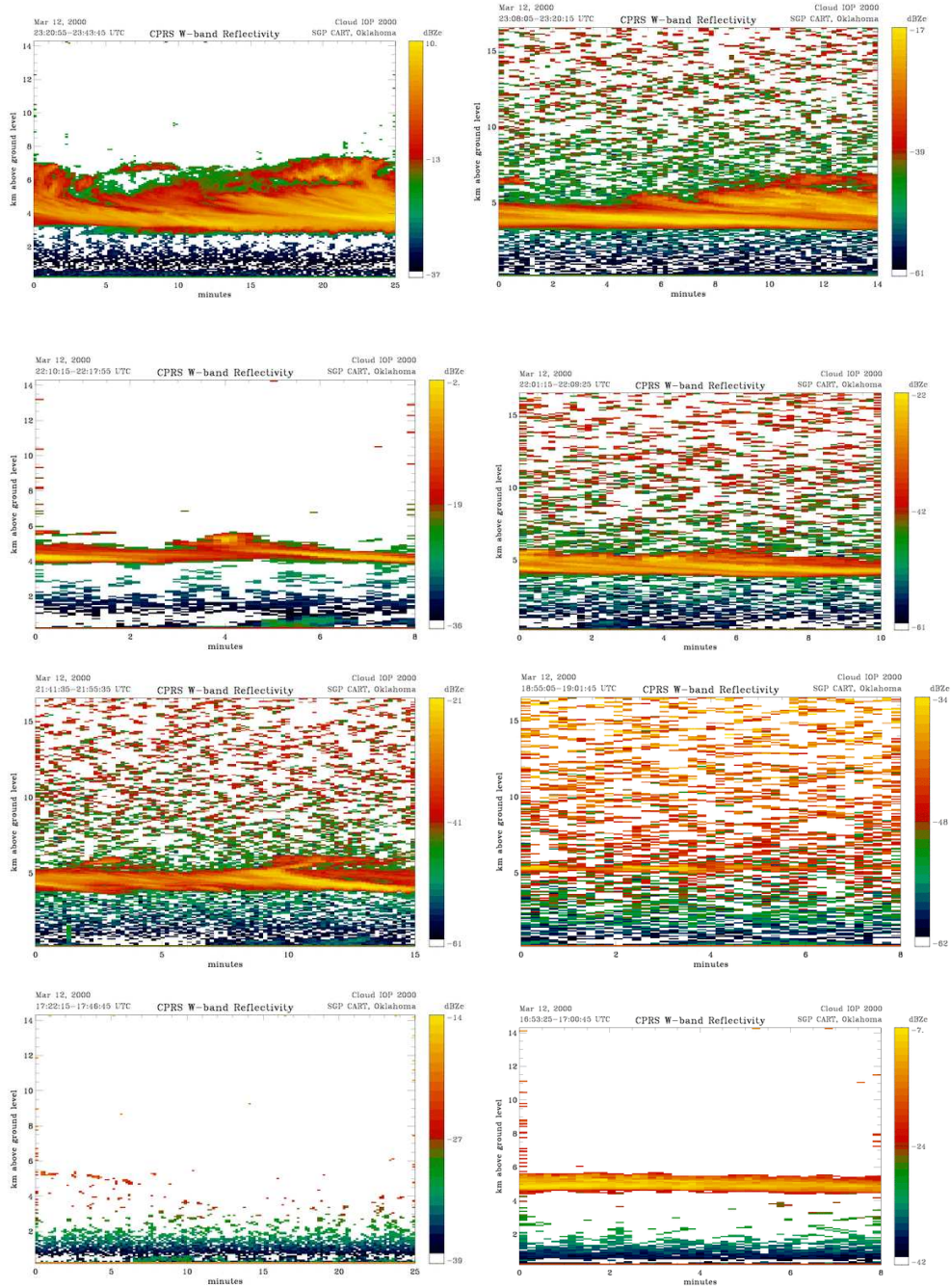
March 5, 2000 at 95GHz



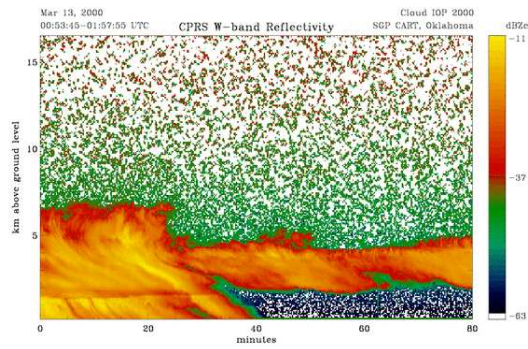
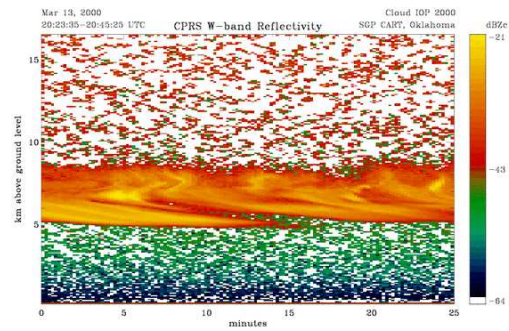
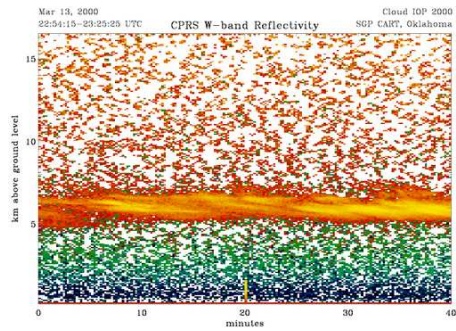
March 9, 2000 at 95GHz



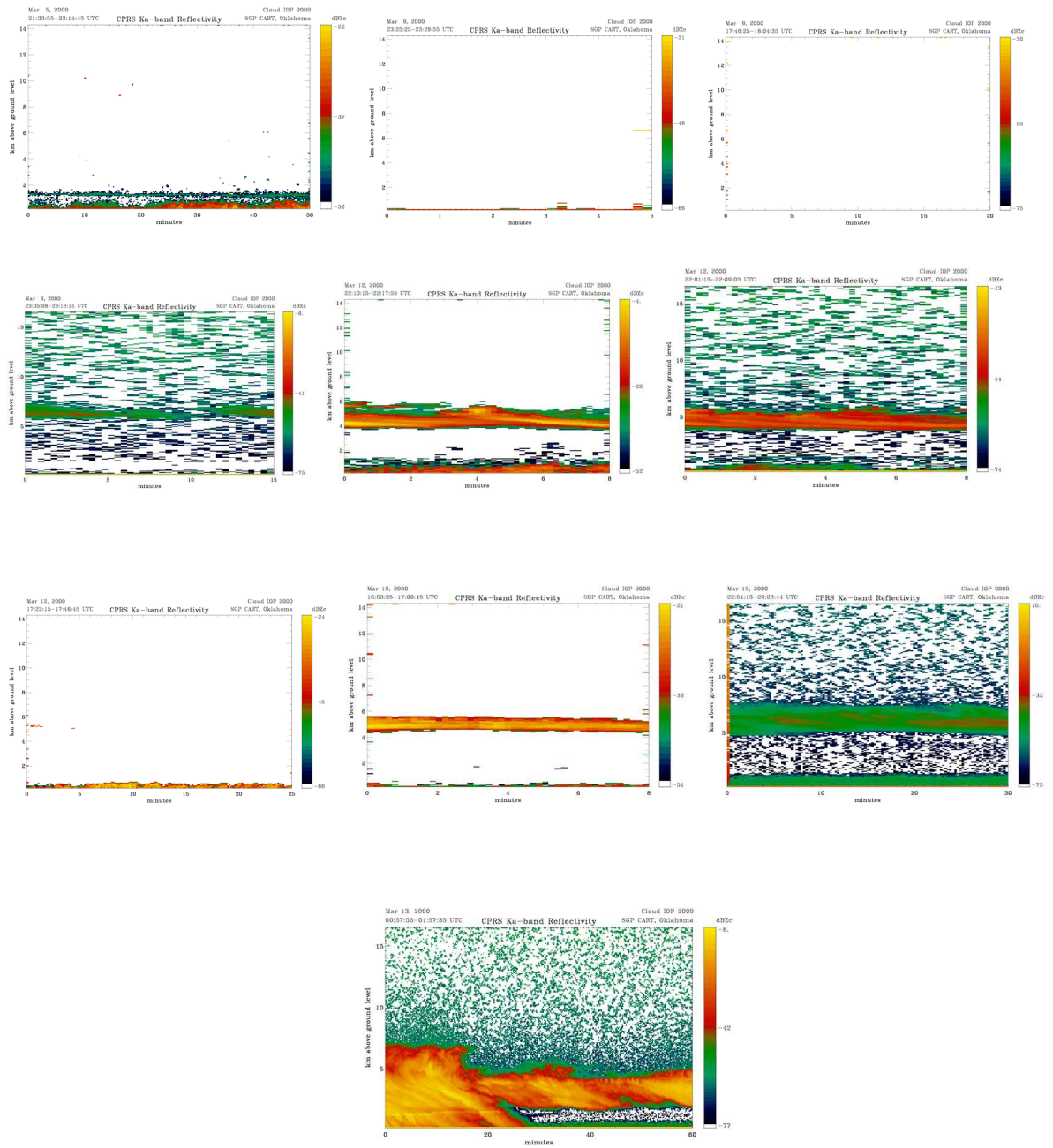
March 12, 2000 at 95GHz



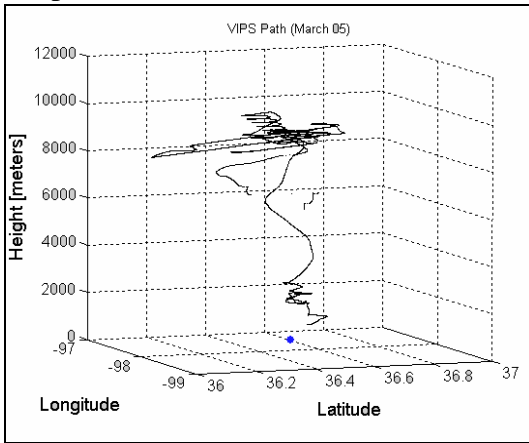
March 13, 2000 at 95GHz



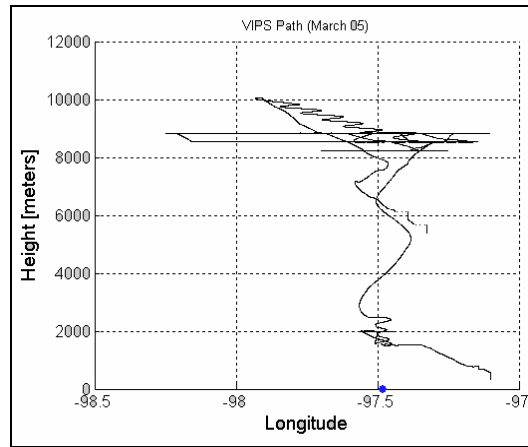
APPENDIX B GRAPHS AT 33GHZ OF LESS RELEVANCE



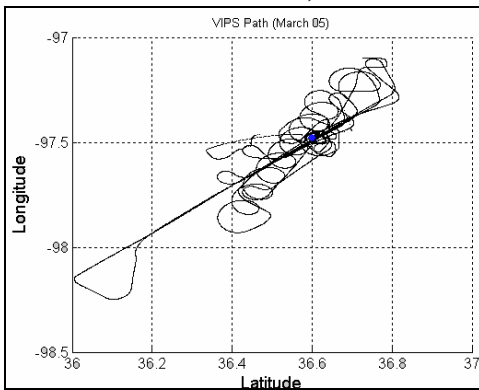
Graphs March 5 2000.



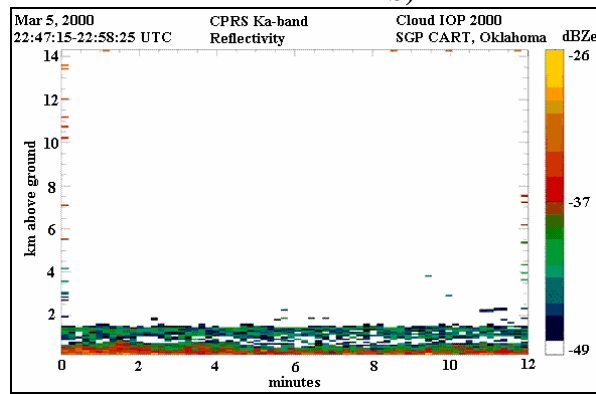
a)



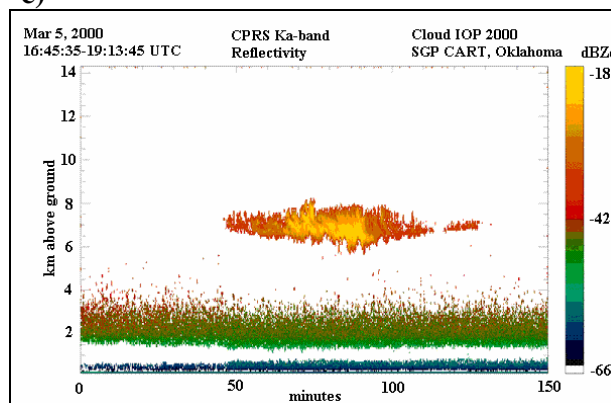
b)



c)



d)



e)

Overhead view of the VIPS flight track pattern for March 13, 2000. The blue dot at (0,0) indicates the position of the CPRS radar, the blue circle is only a reference for data that were spatially closed between sensors; while the colors represent the range of equivalent reflectivity Z_e obtained using a density equation (1). b) Is the same as a) but in three dimensions to show the altitude variation. [ATLAS density]